Improving stability of CO_2 electroreduction by incorporating Ag NPs in N-doped ordered mesoporous carbon structures

Improving Stability of CO_2 Electroreduction by Incorporating Ag NPs in N-doped Ordered Mesoporous Carbon Structures

Järi Van den Hoek[a], Nick Daems[a], Sven Arnouts[a,b], Saskia Hoekx[a,b], Sara Bals[b], and Tom Breugelmans[a]*

[a] Applied Electrochemistry and Catalysis (ELCAT), University of Antwerp, Campus Drie Eiken, Universiteitsplein 1, 2610 Wilrijk, Belgium

[b] Electron Microscopy for Materials Science (EMAT), University of Antwerp, Campus Groenenborger, Groenenborgerlaan 171, 2020 Antwerp, Belgium

*Corresponding author: tom.breugelmans@uantwerpen.be

KEYWORDS

CO_2 electroreduction, electrocatalytic stability, NOMC with deposited Ag NPs, CO production, continuous flow electrolyzer

GRAPHICAL ABSTRACT:

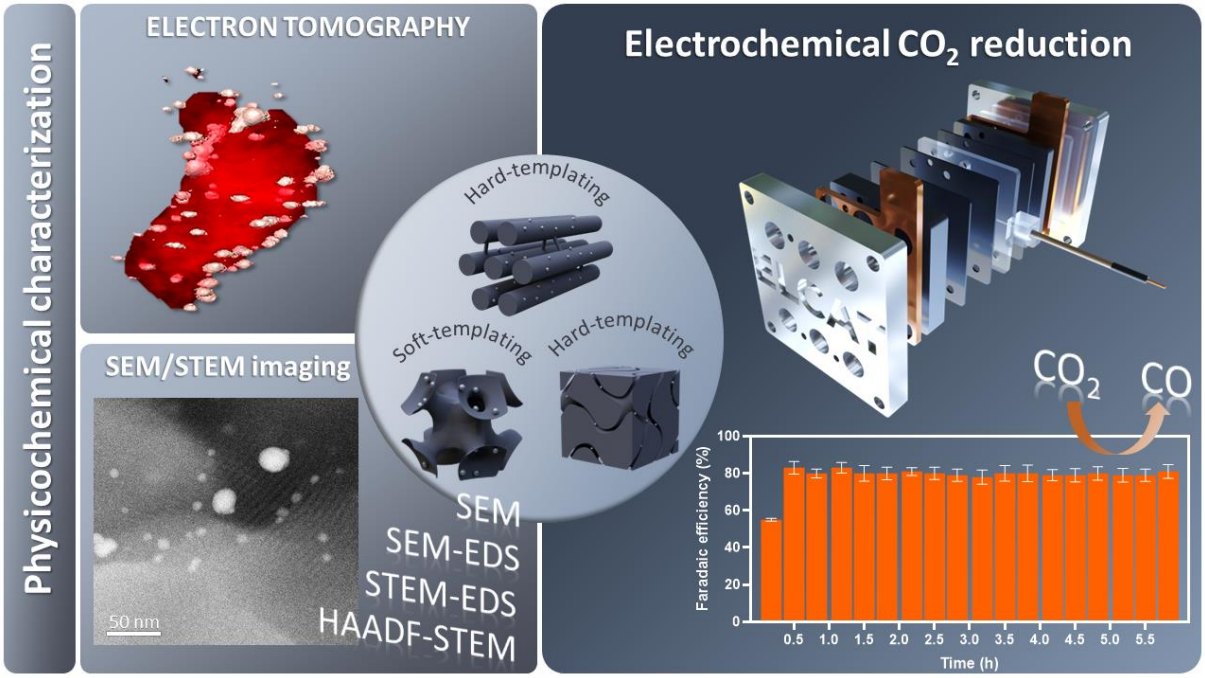

ABSTRACT: The electroreduction of carbon dioxide (eCO_2RR) to CO using Ag nanoparticles as an electrocatalyst is promising as an industrial carbon capture and utilization (CCU) technique to mitigate CO_2 emissions. Nevertheless, the long-term stability of these Ag nanoparticles has been insufficient despite initial high Faradaic efficiencies and/or partial current densities. To improve the stability, we evaluated an up-scalable and easily tunable synthesis route to deposit low-weight percentages of Ag nanoparticles (NPs) on and into the framework of a nitrogen-doped ordered mesoporous carbon (NOMC) structure. By exploiting this so-called nanoparticle confinement strategy, the nanoparticle mobility under operation is strongly reduced. As a result, particle detachment and agglomeration, two of the most pronounced electrocatalytic degradation mechanisms, are (partially) blocked and catalyst durability is improved. Several synthesis parameters, such as the anchoring agent, the weight percentage of Ag NPs, and the type of carbonaceous support material were modified in a controlled manner to evaluate their respective impact on the overall electrochemical performance, with a strong emphasis on the operational stability. The resulting powders were evaluated through electrochemical and physicochemical characterization methods, including XRD, N_2-physisorption, ICP-MS, SEM, SEM-EDS, HAADF-STEM, STEM-EDS, electron tomography and XPS. The optimized Ag/soft-NOMC catalysts showed both a promising selectivity (~80%) and stability compared with commercial Ag NPs while decreasing the loading of the transition metal by more than 50%. The stability of both the 5 wt% and 10 wt% Ag/soft-NOMC catalysts showed considerable improvements by anchoring the Ag NPs on and into an NOMC framework resulting in a 267% improvement in CO selectivity after 72 h (despite initial losses) compared to commercial Ag NPs. These results demonstrate the promising strategy of anchoring Ag NPs to improve the CO selectivity during prolonged experiments due to the reduced mobility of the Ag NPs and thus enhanced stability.

1. Introduction

An active shift from the dwindling supply and polluting nature of fossil fuels to renewable and green energy (wind, solar, and hydropower)[1] is needed to achieve a net zero emissions (NZE) by 2050.[2] While these renewables show promise in tackling the CO_2 emissions resulting from the energy sector (coals, gas, and oil), there is still a need for innovative solutions to reduce the CO_2 emissions of other sectors, such as agriculture and industry, and to reduce the current atmospheric CO_2 levels back to their pre-industrial level. These innovative solutions, such as Carbon Capture Utilization and Storage (CCUS) technologies[3], if successfully implemented, are needed to could help limit the global temperature increase to 1.5 °C.[4] As a highly promising CCU technique, electrochemistry has gained tremendous attention over the past decades because of the various advantages it offers: 1) processing of waste CO_2 directly at point sources or from the atmosphere; 2) production that can be carried out at atmospheric pressure and in an aqueous environment; 3) making use of the intermittency of renewable energy by using it as a power input to drive the reactions and store the energy (temporarily) in chemical bonds; 4) the production of various chemical building blocks, where end products can be easily tailored by varying the electrocatalyst and applied potential.[5,6] One of the most industrially feasible pathways for the eCO_2RR at present is the formation of CO due to its low energy requirement (two moles of electrons per mole of converted CO_2)[7] and the importance of this product as a raw chemical for the production of acetic acid[8,9], phosgene[10], formic acid[11], syngas (consequent potential for application in Fischer Tropsch)[12], and methanol[13]. The production of CO can be selectively achieved by choosing a suitable working potential and electrocatalyst for the eCO_2RR.[14,15] Typical electrocatalysts used for this reduction reaction are Ag[16–18], Pd[19–21], Au[22–24], and Zn[25–28], all of which are reported to yield high FEs towards CO (> 80%) at low overpotentials. However, these metals show suboptimal performance in terms of activity and stability, which impacts the industrial viability of this approach.[29] For this reason, one of the current research approaches is to reduce the (noble) metal content in CO_2 electrolyzers without giving in on activity. Among all transition catalysts, Ag has shown the most potential for further development taking into consideration its price and activity.[30] However, despite the many efforts (e.g. alloying, size and shape optimization) it is still necessary to further improve its activity. We hypothesized that this could be resolved by implementing a co-catalyst such as nitrogen-doped carbons having well-defined surface and microstructural properties. The effects of nitrogen-doped carbon materials on the eCO_2RR are advantageous for the production of CO. Zeng *et al.* obtained a high CO selectivity of 97.8% at -0.86 V vs RHE at a current density of

~7 mA cm^{-2}.[31] Other studies proved the benefits of the combination of Ni and N-doped carbon, resulting in increased activities. For instance, Daems *et al.* were able to synthesize a Ni-N-AC (active carbon) electrocatalyst with a high FE_{CO}, ~98%, at a an applied potential of -0.9 V vs RHE and partial current density of ~24.6 mA cm^{-2}.[32] A step towards industrial productivity was provided by Li *et al.* who reported an FE_{CO} > 80% at 100 mA cm^{-2} with a cell voltage of ~4 V using a Ni/N-C electrocatalyst.[33] The promising performance of these N-doped carbon materials as well as their combination with Ni as a catalyst thus clearly shows the potential impact of combining transition metals with N-doped carbon structures on improving the performance of the eCO_2RR to CO. There is however still room for improvement in terms of Faradaic efficiency (> 80%) towards CO (FE_{CO}) and stability at higher current densities (≥ 100 mA cm^{-2}) in aqueous environments. This study introduces a new approach to take the next step towards industrial feasibility by improving the electrocatalytic stability while maintaining high Faradaic efficiencies at an industrially relevant current density, and at the same time keeping the required amount of the transition metal as low as possible. Herein, an innovative synthesis route is created for optimally depositing small Ag NPs (< 50 nm) in and onto NOMCs prepared via both hard-template (SBA-15 NOMC, KIT-6 NOMC) and soft-template (soft-NOMC, space group: Im-3m) routes using an anchoring agent, i.e. cysteamine and thiourea. These NOMC structures show advantages over carbon black due to the presence of ordered pores and a greater surface area, which improves mass transfer; a nitrogen dopant, which alters the electron density; and provides additional selectivity to CO and an improved stabilization of Ag NPs avoiding agglomeration due to particle confinement.[34] Various synthesis parameters were evaluated (reaction time, anchoring agent, weight percentages of Ag NPs) to improve synthesis pathway to embed the Ag NPs into the NOMC structures. The prepared materials were physicochemically and electrochemically characterized.

The physicochemical and electrochemical screening measurements allowed links to be established between the performance and the electrocatalytic properties, allowing us to determine the optimal synthesis conditions. In the first instance, this optimization was performed on the more readily available carbon black. While the reaction time did not impact performance, a higher Ag loading and the utilization of thiourea as an anchoring agent (instead of cysteamine) resulted in a significant increase in CO selectivity. Ag deposition onto various NOMC materials revealed that the soft-template NOMCs are the most optimal supports due to their straightforward and easily up-scalable synthesis pathway and good performance as an eCO_2RR catalyst. Therefore, these materials were selected for further optimization of the direct

deposition synthesis pathway. The Ag NPs were modified in such a way to yield a final material with an optimal size and interparticle distribution and a homogeneous deposition as this resulted in the highest CO selectivity, while also yielding a clear improvement in stability compared to the bare commercial Ag NPs (improvement of 267% in terms of final selectivity after 72 h). Hence, there is a clear indication that the deposition and distribution of these particles improve the electrochemical selectivity and stability of the eCO_2RR.

2. Experimental section

2.1 Materials and Catalyst preparation

2.1.1 Soft-templating method for NOMC

The NOMC was synthesized according to a report by Wang *et al.*.[35] This soft-templating method created an NOMC with a 3D cubic structure (space group: Im-3m). Firstly, a 5 mL aqueous solution containing 0.470 g of Pluronic F-127 and milliQ was stirred for at least 3 h until a homogeneous state is achieved. Next, 0.654 g 3-aminophenol and 0.420 g hexamethylenetetramine (HMT) were dissolved in 75 mL milliQ in a polypropylene (PP) bottle and stirred for 1 h 30. The 5 mL F-127 solution was added to the latter solution in the PP bottle after which the solution was stirred for 16 h at 50 °C in an oil bath. Afterwards, the PP bottle with the brown solution was placed in the oven for 8 h at 95 °C. The resulting material was then vacuum filtered using a glass Buchner filter (pore size 3) and washed three times with deionized water. The retentate was gathered on an aluminum tray to dry in the oven at 50 °C for at least 8 h. The obtained product was then heated to 800 °C with a heating rate of 1 °C min^{-1} and held at that temperature for 3 h under an Ar atmosphere in a tubular oven (*Fig. S1, Supplementary information*), after which the sample was collected.

2.1.2 Hard-templating method for NOMC

The hard-templated NOMC structures were synthesized according to a study by Sheng *et al.*[36] and Daems *et al.*[37]. Two different silica templates were used, SBA-15 and KIT-6. In a first step, the template walls were covered by an aniline monolayer, which was allowed to polymerize during 24 h. Then, the solvent was removed and the solid samples were pyrolyzed under inert atmosphere at 900 °C for 3 h at a rate of 3°C min^{-1}. In the second step, the remaining pore

volume was filled with dihydroxynaphtalene (DHN). A second heat treatment was performed at 300 °C for 2 h (3 °C min^{-1}) and the sample was washed two times with acetone. The last pyrolysis at 900 °C (5 h, 3 °C min^{-1}) was then carried out, followed by an etching step (NaOH 2 M, 8 h reflux at 100 °C) to remove the template, after which the final material was obtained through filtration (*Fig. S2, Supplementary information*).

2.1.3 Direct deposition of Ag NPs on carbon black

To deposit the Ag nanoparticles on our carbon supports; a general method as described by Kim *et al.* was utilized where the first step is the mixing of a carbon source and an anchoring agent in ethylene glycol (EG).[38] Simultaneously, $AgNO_3$, the silver precursor, was dissolved in ethylene glycol and heated to 50 °C for 20 min. The carbon mixture was added to the silver solution and was stirred for 10 min at 50 °C. The temperature was then gradually increased to 160 °C at a rate of 3-4 °C min^{-1}. The mixture was then stirred for 30 or 60 min, filtered, and washed with isopropanol (IPA). This synthesis pathway resulted in the formation of Ag/C catalysts with various Ag weight percentages, size and interparticle distributions.

2.1.4 Direct deposition of Ag NPs on NOMC

The general method for in-situ incorporation is obtained from Kim *et al.*[38] and Peng *et al.*[39] but was applied with different quantities. Ag NPs were grown onto the NOMC with an $AgNO_3$ precursor with various weight percentages (5, 10, and 15 wt%), anchoring agents (thiourea and cysteamine), amount of anchoring agent (0-3 mg/20 mg_{NOMC}), and reaction times (30 min, 60 min, or 5 h (for the optimized catalysts: Ag/soft-NOMC/5 and Ag/soft-NOMC/10). In order to synthesize 10 wt% Ag NOMC, the following steps were executed; In 35 mL of ethylene glycol, 0.140 g of finely ground NOMC was dissolved with the necessary amount of anchoring agent (cysteamine or thiourea) and sonicated for 30 min until homogeneous and fully dissolved. The $AgNO_3$ precursor was added to 35 mL of EG and slowly heated to 50 °C for a given time (20 or 40 min) while vigorously stirring. Afterwards, the NOMC solution was added, and the mixture was stirred for 10 min prior to being heated to 160 °C with a heating rate of 3-4 °C min^{-1}. After reaching 160 °C, the reaction was allowed to run for 30 min, 60 min, or 5 h. Then, the mixture was cooled down before being filtered with a glass Buchner (pore size 4), washed with IPA, and dried overnight (80 °C; 8 h). The same steps were carried out with different

weight percentages (5, 10, and 15 wt%), and reaction times. This synthesis pathway resulted in the formation of Ag/NOMC catalysts with various Ag weight percentages (*Fig. S3, Supplementary information*).

2.2 Preparation of the Working electrodes

The synthesized Ag-incorporated carbon materials are obtained as a powder. In order to test these catalysts in an electrochemical flow-cell, the powders were dispersed in an ink solution and sprayed onto the microporous layer (MPL) of the gas diffusion electrode (GDE). A stable ink was first prepared by adding 0.038 g of catalyst, a solvent mixture of 0.369 mL MilliQ and 1.403 mL IPA (MilliQ/IPA weight ratio of 25/75) and 0.142 mL Nafion D-520 dispersion (catalyst/Nafion ratio of 85/15) as an ionomer binder. The mixture was sonicated for 1 h using an ultrasonic probe (NexTgen, LAB120) with a frequency of 34 kHz and amplitude of 60%. Subsequently, the mixture was sprayed onto a GDE with an area of 12.5 cm^2 at a temperature of 70 °C using a spray gun. The weight difference before and after was used to calculate the loading of catalyst onto the GDE. This provided us with three 1 cm^2 GDEs, which could be used for testing. We obtained a final catalyst loading of ± 2 mg cm^{-2}.

2.3 Characterization

Inductively coupled plasma mass spectrometry (ICP-MS, Agilent 7500 series) was performed to determine the content of Ag in the carbon materials. Contact angle (CA) measurements were performed to determine the change in hydrophobicity using a Dataphysics OCA 15EC with a drop volume of 5 µL. Crystalline structures of the samples were identified by X-ray diffraction analysis (XRD, Bruker D8 Advance eco) equipped with a Cu Kα radiation (λ = 0.15406 nm, speed of 0.04°/s in the 2θ-area from 5° to 80°). The elemental composition and configuration were studied by X-ray photoelectron spectroscopy (XPS, PHI VersaProbe III) with a monochromatic Al Kα X-ray source (1486.6 eV, 26 eV pass energy, 0.05 eV step size, 100 µm spot size) and an automatic electron neutralizer. The N_2-physisorption measurements were performed using an AUTOSORB-1 version (Quantachrome Instruments) to analyze the NOMC porosity and surface area. The Ag crystallinity, Ag NP morphology, size and distribution across the support as well as the support composition and configuration were determined by scanning electron microscopy (SEM) using a Thermo Fisher Scientific Quanta FEG 250 microscope, high-angle annular dark field scanning transmission electron microscopy (HAADF-STEM) and

electron tomography using a Thermo Fisher Scientific Tecnai Osiris G20 electron microscope operated at 200 kV, energy-dispersive X-ray spectroscopy (EDS) using a ChemiSTEM system.

2.3.1 Electrochemical CO_2 reduction

The eCO_2RR measurements were executed in a custom designed small-scale flow-by reactor. The catholyte and the anolyte were pumped at a flow rate of 2.6 mL min^{-1} to the flow reactor using a peristaltic pump (Ismatec ISM4408). First, a 0.5 M $KHCO_3$ (pH = 8.36) solution was used as catholyte to measure the Ag-based powders with various carbonaceous supports, reaction times, and anchoring agents. Subsequently, the catholyte was changed to a 0.5 M KOH (pH =13.6) solution to measure the Ag-based powders with an soft-NOMC as a support material due to the importance of pH and ohmic drop for improved industrial conditions (lower overpotentials). The catholyte was pumped through the flow reactor to the gas-liquid separator and pumped out of the gas-liquid separator to a waste bottle (single-pass system). A 2 M KOH solution was used as anolyte and was recirculated for all measurements. These two electrolyte chambers were separated by a Nafion-117 cation exchange membrane to allow crossing of cations and provide product separation (detailed set-up information available in *Fig. S4, Supplementary information)*. Furthermore, CO_2 (Air Liquide, 99.999%) was fed to the flow reactor using a Brooks flow controller (GF040, 100 sccm) and the products formed in the CO_2 stream were analyzed using an in-line GC (Shimadzu 2014 series with a TCD detector and a micropacked column (Restek Shincarbon ST, 2 m, 1 mm ID, 100/120 mesh)), which allowed for the detection and quantification of H_2 and CO every 20 min (*Fig. S5, Supplementary information*). The liquid products were analyzed using an HPLC (Waters Alliance HPLC, equipped with a Shodex KC-811 column and a PDA detector (Waters 2996)) (*Fig. S6, Supplementary information*). Ni foam was used as a counter electrode, and a leak-free Ag/AgCl was used as reference electrode (Harvard Apparatus) to control the current and measure the applied potential during all measurements. The Ag-based powders were deposited on a GDE and used as a cathode or working electrode. All samples were measured using chronopotentiometry and cyclic voltammetry using a multi Autolab M204 with a FRA module to determine the ohmic resistance. All applied potentials were converted from Ag/AgCl to the reversible hydrogen electrode (RHE) reference using the following equation.

$$E_{RHE} = E_{ref} + 0.059\,pH + E^{\circ}_{Ag\,/\,AgCl} + iR \qquad [2]$$

Where E_{RHE} and E_{ref} are the potentials versus the RHE and reference electrode (Ag/AgCl), respectively. $E°_{Ag/AgCl}$ is the standard electrode potential of the Ag/AgCl system. iR is the extra potential caused by the ohmic resistance.

3. RESULTS AND DISCUSSION

3.1 Ag NPs on carbon black

The study employed the direct deposition method with commercial carbon black to investigate the influence of the anchoring agents (cysteamine and thiourea), Ag NP loading (5, 10, and 15 wt%), and reaction time (30 vs. 60 min) on Ag particle size, interparticle distance, and loading on the carbon powder (*Table S1, Supplementary information, for full nomenclature: 'Ag'/'carbon substrate'-'targeted weight percentage'/'type of anchoring agent'*). Analysis of the ICP-MS results (Table 1) reveals that, expect for the Ag/C-5/Cy, the actual weight percentages of Ag in the Ag/C samples employing cysteamine as the anchoring agent were consistently lower than their targeted wt%. These deviations are believed to result from losses throughout the synthesis route (e.g. unreacted Ag salts or small unsupported Ag nanoparticles lost during filtration, etc.). Notably, as the initial weight percentages increased to 10 and 15 wt%, the extent of this discrepancy grew larger given the constant reaction time.

Table 1: *Weight percentages of Ag NPs in the Ag/C structures determined by ICP-MS.*

Catalyst	Targeted loading (wt %)	Quantified loading (wt%)
Ag/C-5/Cy	5	5.48
Ag/C-10/Cy	10	7.93
Ag/C-10/Cy/30	10	8.60
Ag/C-15/Cy	15	14.02
Ag/C-10/T	10	6.79
Ag/C-10/T3	10	7.44
Ag/C-15/T	15	11.66

The effect of the particle size on the eCO_2RR to CO has previously been studied by Salehi-Khojin *et al*., and Deng *et al.*. and revealed that Ag nanoparticles with a size smaller than 4-5 nm resulted in a lower eCO_2RR efficiency and an increase in the HER due to the higher proportion of edge sites compared to Ag(100) sites, which negatively affect the catalytic selectivity.[40,41] Targeting a particle size of 5 nm was favored to achieve high catalytic activity for eCO_2RR to CO and enhance Ag NP anchoring on the carbon support materials. To attain the desired particle size, several synthesis parameters were taken in consideration, including the Ag loading, and the reaction time. SEM, SEM-EDS, and HAADF-STEM were utilized to

identify Ag and yield insight into the particle size distribution, and the interparticle distance (Fig. 1a-f). Although SEM/SEM-EDS analysis did not allow for individual Ag particle identification, the presence of Ag on the carbon support was observed (*Figure S7a-d, Supporting information*). HAADF-STEM imaging was conducted to examine Ag NP size and the interparticle distance. Initially, increasing the Ag loading from 5 wt% to 10 wt% resulted in similar particle sizes of 14 ± 7 nm and 16 ± 5 nm, respectively. Further increasing the loading to 15 wt% led to the formation of slightly smaller Ag particles, measuring 6 ± 2 nm. Consequently, no definitive correlation between particle size and loading was observed. Moreover, the reaction time was proven to be an important factor since extending the reaction time from 30 min to 60 min for the 10 wt% Ag/C sample resulted in the formation of larger Ag NPs, with the average size increasing from 4 ± 1 nm to 16 ± 5 nm. This is straightforward, as longer reaction times allow more time for the growth, resulting in larger nanoparticles sizes. Hence, by carefully selecting the appropriate parameters, reaction time and amount of anchoring agent, the synthesis can yield nanoparticles measuring approximately 5 nm in size, thereby validating the efficacy of the synthesis route across all samples, as depicted in Figure 1a-f.

Subsequently, particle dispersion across the support was evaluated by considering both particle size and loading. Increasing the weight percentage of Ag from 5 to 10 wt% resulted in a higher deposition of Ag NPs , leading to denser packing. Further elevating the loading to 15 wt% increased particle loading while reducing interparticle distances, which is detrimental for the stability of the Ag NPs during eCO_2RR as agglomeration would be more facilitated. Consequently, cysteamine has proven to be a promising anchoring agent for obtaining Ag NPs with an optimal particle size (< 20 nm) and a narrow particle size distribution, as was expected based on prior research.[42–44] Despite the promising effects of cysteamine, the molecule size (~ 0.48 nm (H--H, MM2 energy minimization, Chem3D)) and the presence of solely one amine group may pose limitations in synthesizing porous NOMC structures. Therefore, thiourea was proposed as an alternative molecule, having a reduced molecule size (~ 0.35 nm (S--H, MM2 energy minimization, Chem3D)) and two amine groups to interact with the NOMC structure, which should result in a more stable end material and was therefore evaluated next (*Fig. S8a-c, Supplementary information*).

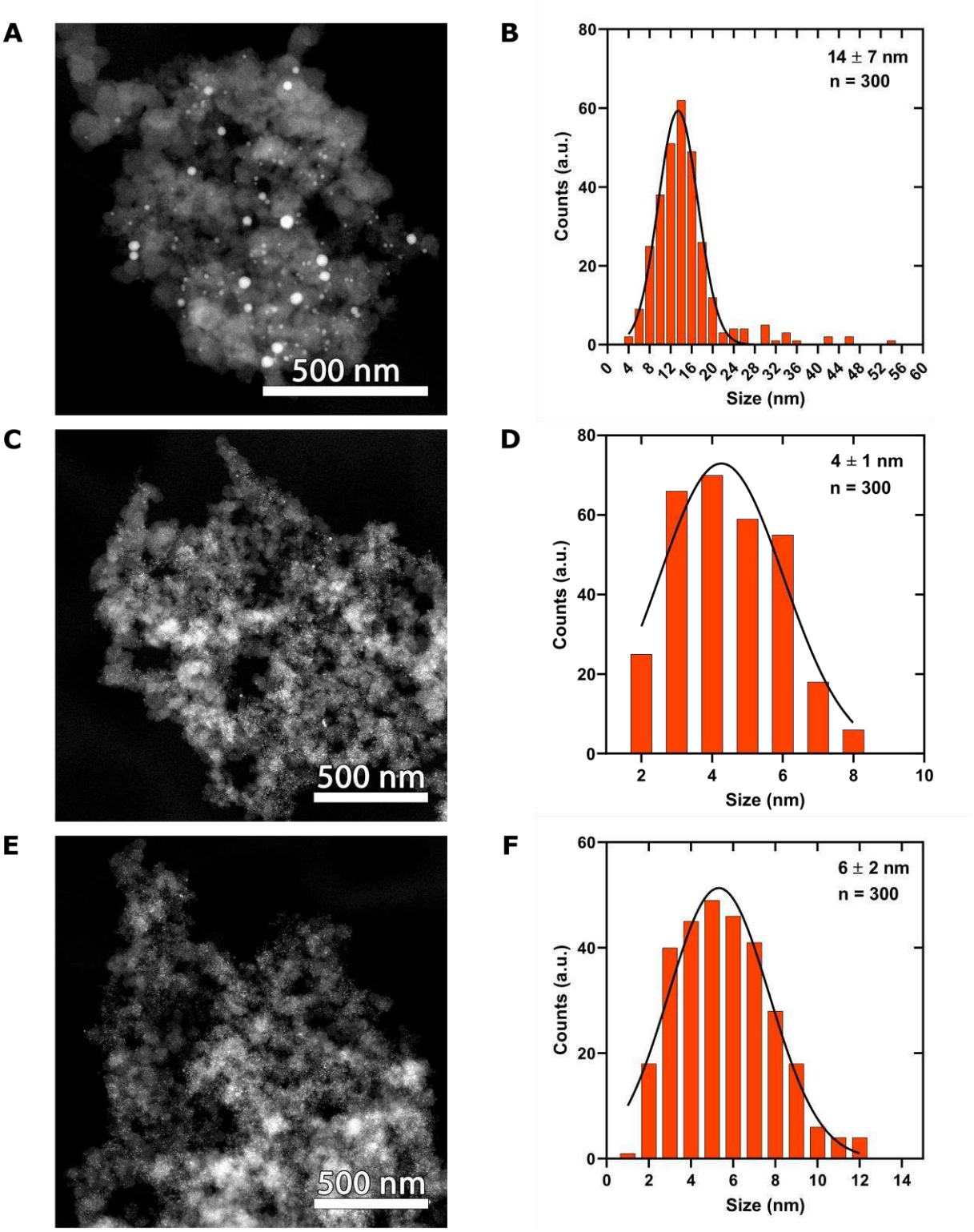

Figure 1: *(A) HAADF-STEM image of Ag/C-5/Cy, (B) Particle size distribution of Ag NPs from Ag/C-5/Cy, (C) HAADF-STEM image of Ag/C-10/Cy/30, (D) Particle size distribution of Ag NPs from Ag/C-10/Cy/30, (E) HAADF-STEM image of Ag/C-15/Cy, and (F) Particle size distribution of Ag NPs from Ag/C-15/Cy. A reaction time of 60 min was used for Ag/C-5/Cy, and Ag/C-15/Cy. A reaction time of 30 min for Ag/C-10/Cy/30.*

Initial ICP-MS analysis revealed a higher deviation of Ag content compared to the powders with cysteamine (Table 1). This deviation suggested higher losses of Ag NPs during synthesis. Additionally, larger particle sizes were obtained for Ag/C-10/T, 48 ± 16 nm, compared to Ag/C-10/Cy, 16 ± 5 nm as evidenced by the HAADF-STEM images (Fig. 2). An increase in the loading of Ag to 15 wt%, 52 ± 11 nm, did not result in a significant change in particle size. We believe that the increased particle size stems from the different molecular structure of thiourea.

Indeed, thiourea, unlike cysteamine, features a sulfur atom not bound to a hydrogen atom (making it free for interaction) but doubly bound with a carbon atom. This structural difference affects electron density and geometry. Moreover, Thiourea contains a thioamide group, enabling thione and thiol tautomerization with a strong negative charge on the sulfur group in the thiol form. These factors alter the interaction with Ag ions, leading to larger nanoparticles (*Fig. S9a-f, Supplementary information*). This was confirmed by increasing the amount of thiourea to 3 mg / 20 mg_C, which resulted in the formation of even larger particles up to 1.8 µm (*Fig. S9a-b, Supplementary information*). Despite, the formation of larger particles, thiourea showed potential as an anchoring agent. A further optimization of the reaction time and the amount of reagents should provide Ag NPs, which are comparable in size with the ones synthesized using cysteamine (5 – 15 nm), and obtaining the targeted Ag weight percentages, respectively. Given the stronger interaction that is expected between thiourea and Ag as compared to cysteamine, all further experiments were performed utilizing thiourea as anchoring agent as we believe a stronger interaction will result in a higher stability (less mobility of the particles).

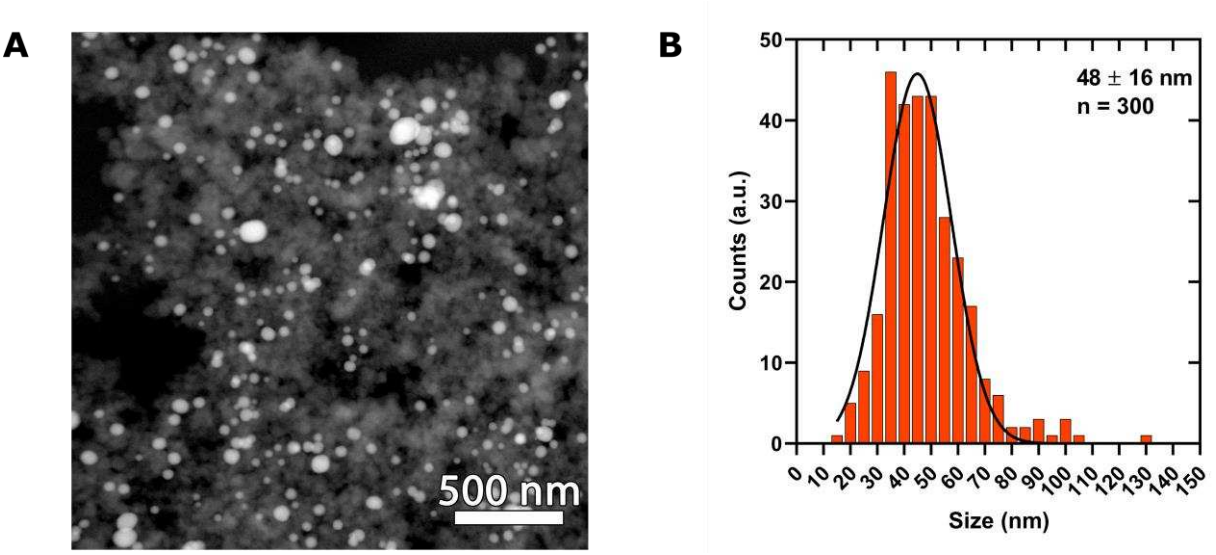

Figure 2: *(A) HAADF-STEM image of Ag/C-10/T, and (B) Particle size distribution of Ag from Ag/C-10/T. A reaction time of 60 min was used for Ag/C-10/T.*

3.2 NOMC structures

The NOMC materials were made using two synthesis routes: hard-templating and soft-templating. The hard-templating route was used for the synthesis of SBA-15 NOMC and KIT-6 NOMC, which have the negative of a P6mm and Ia$\bar{3}$d space group, respectively, while the soft-templating method was used for the synthesis of a structure with an Im$\bar{3}$m space group (*Fig. S10, Supplementary information*). The strength of these NOMC materials is their three dimensional structure with tunable mesopore sizes, enhancing surface area, and facilitating reactant transport to active sites. Furthermore, nitrogen dopants in the NOMC structure create active sites for eCO_2RR, due to a shift in electron density of the material.

The surface area, pore size, and pore volume of the final materials were determined using nitrogen physisorption (Table 2 and *Fig. S11-S13, Supplementary information*). Based on this data, it is clear that all NOMC structures were successfully obtained. The most crucial parameter for the subsequent incorporation of the Ag NPs is the NOMC pore size, which should ideally be as large as possible to allow an efficient incorporation of as much Ag as possible. KIT-6 NOMC demonstrated the largest pore diameter, making it a suitable material to allow an easier accommodation and confinement of said Ag NPs (*vide infra*).

Table 2: *N_2-physisorption analysis of the different synthesized carbon structures from the characterization of BET surface area, pore volume, and average pore radius. Average values were given for soft-NOMC and SBA-15 NOMC as various batches were prepared throughout this experimental study.*

Carbon structure	S_{BET} (m^2/g)	V_{pores} (cm^3/g)	Avg. pore diameter (nm)	Ref.
SBA-15 NOMC	788 ± 89	0.6 ± 0.1	3.2 ± 0.1	This work
KIT-6 NOMC	739.109	1.343	7.266	This work
Soft-NOMC	499 ± 148	0.32 ± 0.09	2.6 ± 0.2	This work
Carbon black XC72	230	/	/	[45]

Despite resulting in the lowest average pore diameter, the soft-templating synthesis offered practical advantages, considering it consists of an easier, robust and more easily up-scalable approach towards NOMCs as compared to the more time-consuming and tedious hard-

templating method. The surface area was still improved from 230 $m^2\ g^{-1}$ for carbon black to 499 ± 148 $m^2\ g^{-1}$ for the soft-NOMC structure and should thus improve the Ag NP deposition approach. Next, the different NOMCs were also evaluated for the presence of ordered pores and the uniformity of their structure using HAADF-STEM (Fig. 3a-c). The three NOMCs showed an uniform structure in line with their expected space group. Furthermore, the presence of mesopores was confirmed and their diameter corresponds well to the values obtained by nitrogen physisorption, i.e.~3 nm for the SBA-15 NOMC,~7 nm for the KIT-6 NOMC, and ~3 nm for the soft-NOMC.

By using aniline as a nitrogen source, nitrogen moieties were also incorporated into the final material as they were expected to improve the catalytic performance for the eCO_2RR. To determine the amount and the configuration of nitrogen inside the carbon framework (i.e. pyrrolic, graphitic, pyridinic, and oxidized pyridinic, *Fig. S14-S15, Supplementary information*), the samples were analyzed using XPS. The result of the soft-NOMC structure (Figure 3d), showed the presence of mainly graphitic (2.88 wt%) and pyridinic (1.34 wt%) nitrogen with pyridinic nitrogen being the most known nitrogen configuration of the two to improve the catalytic performance of the NOMC. Indeed, this was established by Wu *et al.* who stated that the highest catalytic performance can be obtained when a high presence of pyridinic and pyrrolic nitrogen is present.[46,47] Despite a lower pyridinic nitrogen content, i.e. 0.16 wt%, SBA-15 NOMC contained a high pyrrolic nitrogen content (i.e. 1.82 wt%), which was also proven to be active for the eCO_2RR to CO. The combined presence of active pyridinic and pyrrolic nitrogen was higher compared to the soft-NOMC, 1.39 wt%, thus resulting in a further increase in catalytic activity towards CO. Furthermore, the incorporation of nitrogen in the KIT-6 NOMC was the least successful despite the time-demanding synthesis procedure. When taken together it is clear that the active N content of SBA-15 NOMC is higher than that of soft-NOMC. Consequently, the activity of the bare soft-NOMC is expected to be significantly lower than that of SBA-15 NOMC (*vide infra*). For this reason, the impact of the Ag incorporation and its parameters (size, content, distribution, etc.) on the overall eCO_2RR performance was expected to be larger and easier to follow on soft-NOMCs. Together with their more straightforward synthesis approach this made them the most promising material for further investigation.

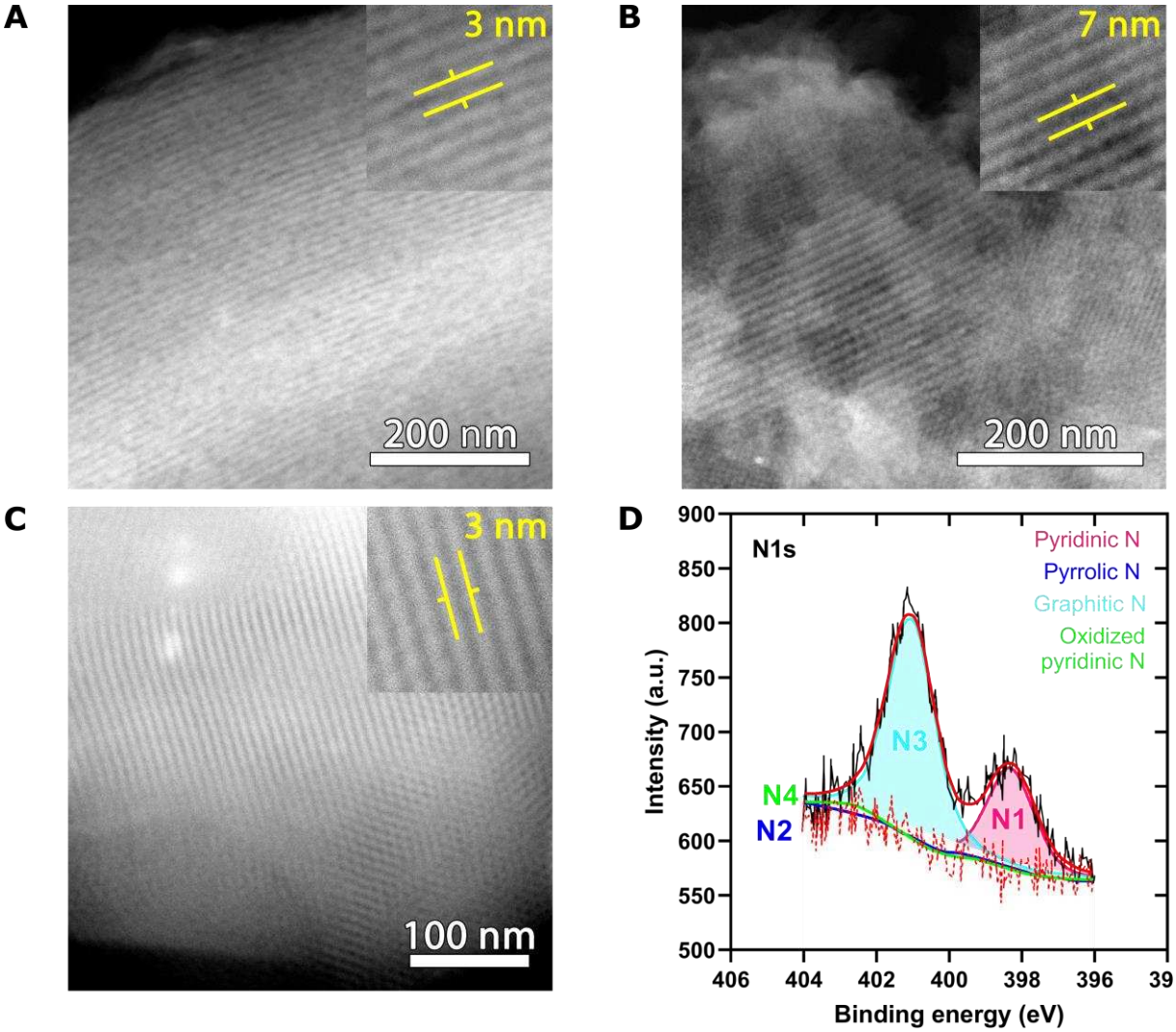

Figure 3: *(A) HAADF-STEM image of a SBA-15 NOMC structure, (B) HAADF-STEM image of a KIT-6 NOMC structure, (C) HAADF-STEM image of a soft-NOMC structure, and (D) Deconvoluted N1s XPS spectra of a soft-NOMC with pyridinic nitrogen (N1) at 398.2 eV, pyrrolic nitrogen (N2) at 399.5 eV, graphitic nitrogen (N3) at 400.6 eV, and oxidized pyridinic (N4) at 402.5 eV.*

3.3 Ag NPs deposited on NOMC structures

Ag NPs were incorporated onto NOMC structures, by utilizing the optimal settings established for carbon black, employing the direct deposition method with thiourea as the anchoring agent and a reaction time of 30 min. The targeted loading was set at 10 wt% due to an optimal balance between the amount of Ag NPs and activity for eCO_2RR, as presented in Table 3. In the case of hard-templating NOMC structures, the actual loading, as determined by ICP-MS, closely matched the targeted value, deviating by less than 2 wt%. However, the Ag loading for the Ag/soft-NOMC was significantly lower, i.e. only 4.06 wt%. We attribute this difference to

greater losses of small nanoparticles (< 20 nm) due to lower quantity of anchoring agent used for the soft-NOMC structure (1 mg/20 mg_{NOMC} vs 3 mg/20 mg_{NOMC}). As stated in section 3.1, a higher amount of thiourea resulted in the formation of larger particles (> 200 nm), which were harder to lose during synthesis compared to the smaller particles (< 100 nm) obtained with a lower amount of anchoring agent. The smaller particles were desired, which is why the anchoring agent content was lowered for the optimal soft-NOMC material.

Table 3: *Weight percentages of Ag NPs in the Ag/NOMC structures determined by ICP-MS.*

Catalyst	ICP-MS (wt%)
Ag/soft-NOMC	4.06
Ag/SBA-15 NOMC	10.27
Ag/KIT-6 NOMC	8.00

Next, the various Ag/NOMC powders were characterized using HAADF-STEM and STEM-EDS to determine the particle size distribution. The Ag particles were visualized using HAADF-STEM in Figure 4a-c for the Ag/NOMC structures. The Ag/SBA-15 NOMC shows large Ag particles or clusters (up to 260 nm) in combination with a distribution of smaller particles (~50 nm). STEM-EDS imaging confirms the presence of Ag NPs and shows an exact overlap of Ag and S signal, proving the interaction between the anchoring agent and the Ag nanoparticles (*Figure S16a-e, Supplementary information*). The particles of the Ag/KIT-6 NOMC were similar in terms of particle size, 210 ± 114 nm, with a wide Gaussian distribution. The Ag/soft-NOMC consisted of various large particles or clusters with a significant amount of smaller particles distributed over the surface of the NOMC structure as well as in the porous structure, clearly indicating the advantage of using a lower amount of anchoring agent in combination with soft-NOMC.

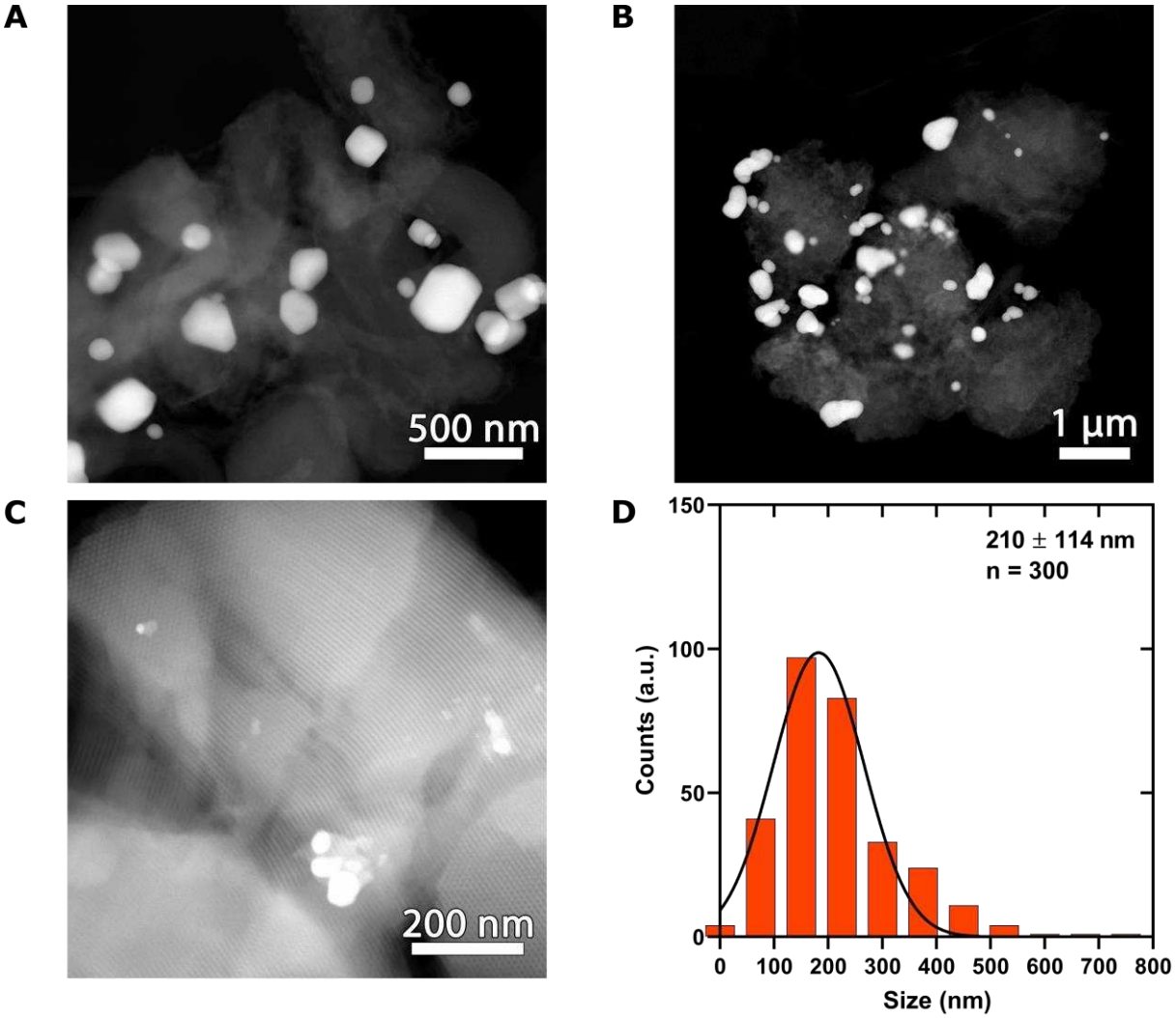

Figure 4: *(A) HAADF-STEM image of a Ag/SBA-15 NOMC structure, (B) HAADF-STEM image of a Ag/KIT-6 NOMC structure, (C) HAADF-STEM image of a Ag/soft-NOMC structure, and (D) Particle size distribution of an Ag/KIT-6 NOMC structure. A reaction time of 30 min was used for Ag/SBA-15 NOMC, Ag/soft-NOMC, and Ag/KIT-6 NOMC.*

3.4 Optimization of the direct deposition on a soft-NOMC

A further optimization was essential to obtain an improved particle size and interparticle distribution. Because of the reasons mentioned above (i.e. straightforward synthesis, high pyridinic N content, high surface area and relatively easy incorporation of Ag also in the inner pore structure), the Ag/soft-NOMC was investigated further and the optimization of the Ag NP deposition was performed in more detail by fine-tuning the amount of thiourea and improving the particle size and interparticle distribution. The amount of thiourea was lowered to 0.175 mg / 20 mg_{NOMC} for the 5 wt% Ag/soft-NOMC (referred to as Ag/soft-NOMC/5) and 0.350 mg/ 20 mg_{NOMC} for the 10 wt% Ag/soft-NOMC (referred to as Ag/soft-NOMC/10). The abundant

presence of thiourea could otherwise result in two adverse consequences. Firstly, the elevated amounts of thiourea enhances the tendency for self-interaction among thiourea molecules, thereby diminishing the stabilization of the Ag ions, resulting in the formation of larger particles (*see section 3.1*). Consequently, the available active surface area would decrease, exerting a negative influence on the activity and/or the selectivity during the eCO_2RR. Secondly, high amounts of thiourea were also anticipated to shield the pyridinic nitrogen moieties from participating in the reaction. For these reasons, a lower amount of thiourea was expected to yield favourable outcomes. Our study, supported by ICP-MS data and HAADF-STEM images, underscores the pivotal role of achieving the right balance in thiourea amounts. Complete elimination of thiourea (Ag/soft-NOMC/10NT) was found to result in a significant reduction in the incorporation of Ag NPs, with an underwhelming 0.87 wt% Ag content, falling short of the targeted 10 wt% (*Fig.S17a-b, Supplementary information*). Thus, it is evident that the precise control of thiourea concentration is indispensable for the successful deposition of Ag NPs and the formation of particles of the desired size.

The resulting Ag/soft-NOMC catalysts were analyzed using ICP-MS, HAADF-STEM and STEM-EDS, as shown in Figure 5a-d. The actual weight percentages determined by ICP-MS were 4.93 wt% and 9.63 wt% for Ag/soft-NOMC/5 and Ag/soft-NOMC/10, respectively, indicating a significant reduction in Ag losses compared to the non-optimized Ag/soft-NOMC. The optimized Ag/soft-NOMC catalyst with 5 wt% showed an excellent particle size distribution ranging from 4 nm to 40 nm (see Figure 5a). The 10 wt%, however, showed a larger particle size distribution with the presence of smaller particles (< 50 nm) and some larger clusters (> 200 nm) resulting in a less optimal size distribution of Ag NPs. Also this is an improvement as compared to before the optimization procedure, clearly showing the benefits of this step.

Electron tomography further confirmed the presence of Ag NPs within the mesopores of the NOMC material. Ortho-slices were taken approximately halfway through the reconstructed volume, which confirm the presence of Ag NPs in the middle of the NOMC volume (Figure 5e-f). Ag/soft-NOMC/5, in particular, displayed medium-sized particles (~50 nm) incorporated within volume of the NOMC material. While these particles were not stabilized in the pores of the structure, they were still supported due to incorporation into the volume of the NOMC material itself. In contrast, Ag/soft-NOMC/10 contained a greater fraction of large particles on the outer surface of the structure. The latter are considered to be able to move freely during the

CO_2RR and are expected to suffer a more significant performance loss throughout the reaction. Nevertheless, the utilization of the inner structure by the smaller and the medium Ag NPs for Ag/soft-NOMC/5 and the smaller Ag NPS for Ag/soft-NOMC/10 results in a better coverage and distribution in the carbon framework, which should lead to an improved stability of these NPs. Besides the influences of particle size and interparticle distance, the crystallinity has proven to be a determining factor for the eCO_2RR. Nevertheless, in this specific case, HR-STEM images showed the presence of a polycrystalline structure comparable to commercial Ag, which was further confirmed by XRD due to the identical 2θ-peaks of the crystallographic planes (111) at 37.7°, (200) at 43.9°, (220) at 64.1° , and (311) at 77.0° *(Figure S18a-d, Supporting information)* and will thus not influence the performance in our case. The optimization process, which resulted in smaller particle size distributions, improved incorporation, and the presence of a polycrystalline structure, is expected to significantly enhance selectivity, activity, and overall stability (vide infra).

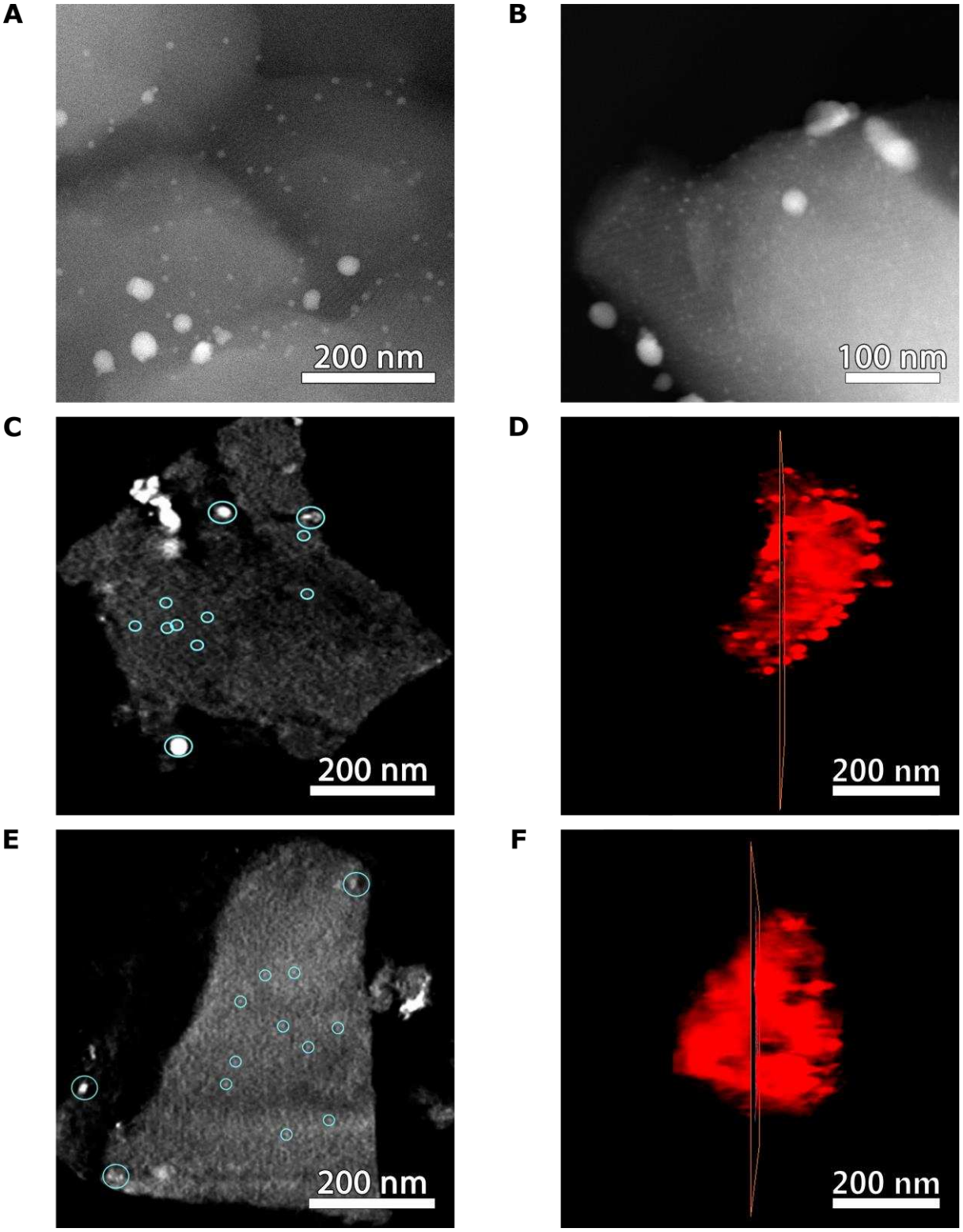

Figure 5: *(A) HAADF-STEM image of an Ag/soft-NOMC/5 structure, and (B) HAADF-STEM image of an Ag/soft-NOMC/10 structure. (C) Orthoslice in the xz direction approximately halfway through the volume from a 3D reconstruction of an Ag/soft-NOMC/5 structure (Movie S1), (D) Orthoslice position in the 3D volume of the Ag/soft-NOMC/5 structure, (E) Orthoslice in the xz direction approximately halfway through the volume from a 3D reconstruction of an Ag/soft-NOMC/10 structure (Movie S2), and (F) Orthoslice position in the 3D volume of the Ag/soft-NOMC/10 structure.*

3.5 Electrochemical CO_2 reduction

Catalyst performance relies on material characteristics (e.g. particle size, interparticle distance, loading, anchoring agent) and experimental parameters (e.g. applied potential, CO_2 feed rate, reactor setup). In this study, the latter remained constant, as these process conditions, determined in our previous work, were favorable for CO production and to evaluate catalysts performance in the present work.[48] The synthesized Ag/C and Ag/NOMC powders were tested in a small-scale flow-by electrolyzer for their activity and selectivity towards CO.

Initially, the Ag/C powders obtained using the direct deposition method on carbon black with cysteamine as anchoring agent were analyzed for one hour at 100 mA cm^{-2}. Regardless of the weight percentages used, FE_{CO} remained ~80, though variances in potential were observed (Figure 6a-b). Higher Ag loading (10 wt%) resulted in a lower potential (i.e. 130 mV lower overpotential), highlighting the importance of electrochemical active surface area. Indeed, in order to maintain a certain current density a higher potential is required for lower Ag weight percentages. The highest potential was indeed obtained with the Ag/C-5/Cy catalyst, i.e. -0.76 ± 0.05 V vs RHE, and was a result of its low electrochemical active surface area (i.e. it had the lowest Ag loading, namely 5.48 wt%). Further increasing the loading to 15 wt% showed diminishing returns as a plateau appeared and the potential did not drop further. The inclusion of these sub-20 nm nanoparticles in the Ag/C catalyst unequivocally enhances the electrochemical surface, a pivotal factor in facilitating catalytic reactions, thereby exerting a positive influence on the overall catalytic activity of Ag/C catalyst.[49] Subsequently, the reduction of the reaction time on performance was investigated. Lowering the reaction time from 60 min to 30 min resulted in a reduced FE_{CO} by 6% (i.e. from 80 ± 1% to 74 ± 1%) and an increase in FE_{H2} by 2%. The reason for this is the strong reduction in particle size to 4 ± 1 nm, which is close to or below the optimal value of 5 nm and might explain an increased tendency for hydrogen evolution. The potential, on the other hand, does not alter upon reducing the reaction time, indicating the dominant role of Ag loading.

The transition to thiourea as an anchoring agent resulted in larger particles (~ 50 nm) during the direct deposition of Ag NPs on the carbon black. This change in particle size from < 20 nm to ~50 nm did not impact the eCO_2RR (Ag/C-10/Cy and Ag/C-10/T in Figure 6a). Indeed, when comparing both samples it was clear that the sample prepared with thiourea showed a similar activity and selectivity towards CO (i.e. 80 ± 2% vs. 80 ± 1% with cysteamine). Furthermore,

563 despite the presence of similar sized nanoparticles for Ag/C-15/T, their selectivity is improved
564 as compared to Ag/C-10/T because of its higher potential increasing the CO_2 reduction rate at
565 the cost of the hydrogen evolution reaction. Nevertheless, these larger particles are undesired
566 as they result in a lower mass activity and will be less efficiently incorporated in our NOMC
567 structures.
568
569 Finally, the potential was around 190 mV more negative when using an increased amount of
570 thiourea (1 mg/ 20 mg_C to 3 mg/ 20 mg_C). This is believed to have two main causes: (1) the
571 presence of larger Ag NPs (> 100 nm), and (ii) the thiourea blocking active sites due to its better
572 interaction with the Ag NPs (as discussed previously) both lowering the available
573 electrochemical active surface area as such explaining the observed shifts in potential. It was
574 thus clear that adding high amounts of thiourea is detrimental for the activity as it reduces the
575 available electrochemical active surface area by generating more large particles and blocking
576 active sites, as previously shown in Figure S8. However, despite the negative effect on the
577 activity, the selectivity towards CO improved to 86 ± 2%, which we believed to be due to the
578 higher potential required for this sample. Despite the increased particle size and the lower
579 loading of Ag compared to cysteamine, thiourea showed to provide a similar activity and
580 selectivity towards CO. Adding this to our belief that thiourea would form a stronger interaction
581 with the Ag NPs and improve stability, made us select thiourea for further experiments.
582
583

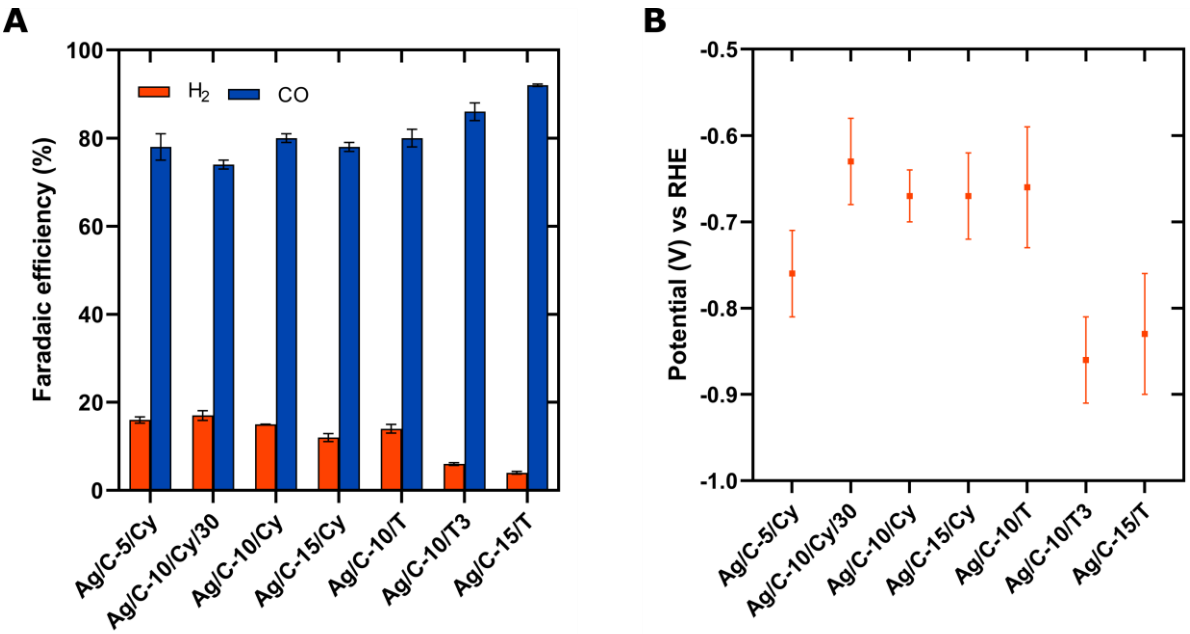

584

Figure 6: *(A) The average Faradaic efficiencies for H_2 and CO at 50 min in a small-scale flow-by electrolyzer at a current density of 100 mA cm^{-2} with 0.5 M $KHCO_3$ as catholyte, 2.0 M KOH as anolyte and a CO_2 flow of 25 mL min^{-1}. The remaining Faradaic efficiencies are assigned to formic acid resulting in a ~100% total Faradaic efficiency. (B) The average potential (V) vs RHE over 50 min obtained while measuring the Ag/C samples at a current density of 100 mA cm^{-2} with 0.5 M $KHCO_3$ as catholyte, 2.0 M KOH as anolyte and a CO_2 flow of 25 mL min^{-1}. A reaction time of 60 min was used for Ag/C-5/Cy, Ag/C-10/Cy, Ag/C-15/Cy, Ag/C-10/T, Ag/C-10/T3, and Ag/C-15/T. A reaction time of 30 min was used for Ag/C-10/Cy/30.*

Subsequently, we investigated the influence of the different supporting materials, i.e. carbon black and NOMCs, on the selectivity and activity of the eCO_2RR parameters (Figure 7a-b). Carbon black is known for primarily producing H_2 with minimal CO production (FEs: 87 ± 4% for H_2 and 13 ± 1% for CO). When transitioning to NOMC structures, different results were expected as a consequence of the increased surface area and the incorporation of active N sites. This effect, however, was not as pronounced for all NOMCs.

The KIT-6 NOMC and especially the SBA-15 NOMC displayed enhanced eCO_2RR performance with higher selectivity towards carbon products. The soft-NOMC showed a slight decrease in selectivity, but this was primarily in the initial phase (Figure 9a), indicating a higher selectivity for CO than C. However, its three dimensional pore structure resulted in longer diffusion times of CO from the active sites, leading to lower initial selectivity (Figure 8a). The lower potential of these NOMC structures was a consequence of the increased electrochemical active surface area. KIT-6 NOMC, on the contrary to soft-NOMC and SBA-15 NOMC, resulted in a significant selectivity towards formate, i.e. FE of 23.21 ± 0.04%, besides producing CO (FE of 14 ± 3%). Although the reason behind this remains unclear, we believe it was likely a result of a combination of a different nitrogen configuration and the 3D cubic morphology of KIT-6 NOMC, which somehow helped to stabilize the CO_2 intermediate using multiple active nitrogen sites, resulting in a change in pathway with the formation of formate as a result. Further research is necessary to fully elucidate this reason but is not part of the scope of this work. Finally, SBA-15 NOMC showed the highest selectivity towards CO, 68.6 ± 0.3%, and the lowest potential, -0.78 ± 0.01 V vs RHE, which was believed to be due to the high presence of active nitrogen sites and the presence of a straight, 2D hexagonal pore structure allowing smooth entry of reactants and removal of products.

Subsequently, the Ag-based catalysts were tested under the uniform conditions (Figure 8a-b) and displayed enhanced activity and selectivity. Notably, Ag/KIT-6 NOMC provided the

highest CO selectivity ,reaching 84 ± 1% compared to 73 ± 2% and 74 ± 2% for Ag/SBA-15 NOMC and Ag/soft-NOMC, respectively. The superior catalytic performance of Ag/KIT-6 NOMC results from its larger average pore diameter, providing the Ag NPs more surface area to be deposited on and the easier transport to and from active sites. Therefore, a greater interparticle distance, improved average particle size, and higher electrochemical active surface area was obtained, resulting in improved CO selectivity and activity (Figure 4b). All three Ag/NOMCs demonstrated comparable and improved activity (overpotential), underscoring the beneficial influence of Ag. The slightly lower selectivity of Ag/SBA-15 NOMC was attributed to the formation of larger particles, which negatively influenced the CO selectivity.[40] For the Ag/soft-NOMC, a comparable selectivity was obtained but this is ascribed to the lower weight percentage (4.06 wt%) and the larger fraction of bigger particles as compared to KIT-6 NOMC. These results highlight the potential of doped ordered mesoporous carbon materials as an active support, owing to their larger surface area, ordered mesoporous structure and the presence of a dopant in contrast to plain carbon black. Despite slightly lower performance as compared to Ag/KIT-6 NOMC, Ag/soft-NOMC was chosen for further Ag incorporation optimization, primarily due to its more straightforward and scalable synthesis as discussed in section 3.3.

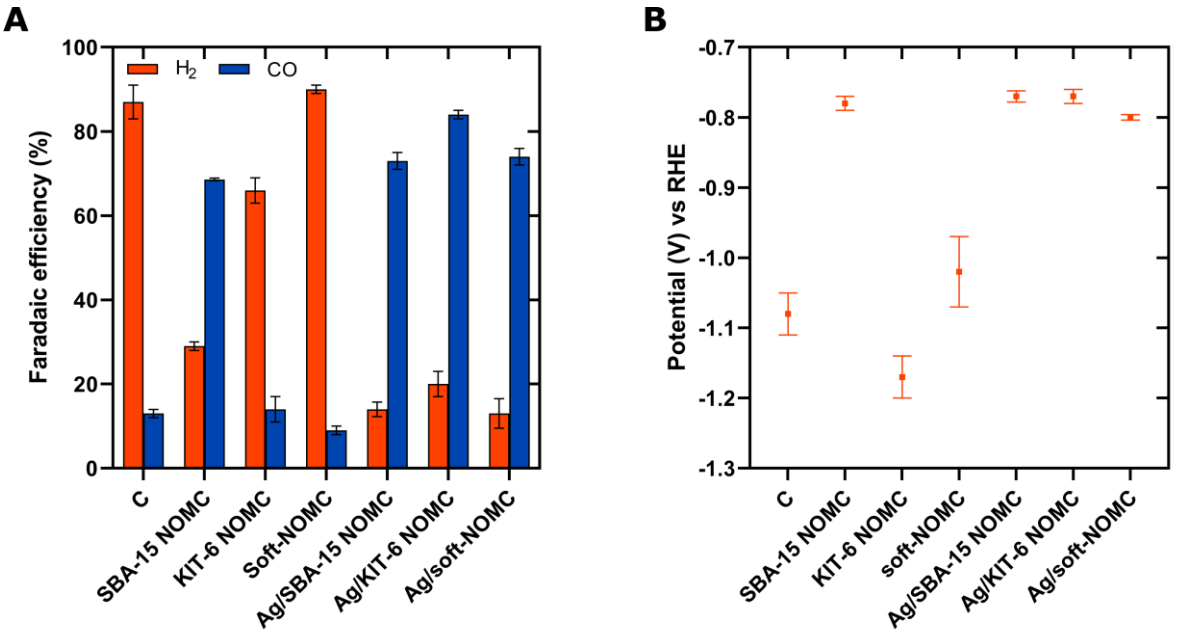

Figure 7: *(A) The average Faradaic efficiencies for H_2 and CO at 50 min for the different catalysts: carbon black, NOMC structures, and Ag/NOMCs. The remaining Faradaic efficiencies are assigned to formic acid resulting in a ~100% total Faradaic efficiency. (B) The average potential (V) vs RHE over 50 min for the different catalysts: carbon black, NOMC structures, and Ag/NOMCs. This data was obtained while measuring the Ag/C samples at a current density of 100 mA cm^{-2} with 0.5 M $KHCO_3$ as catholyte, 2.0 M KOH as anolyte and a*

CO_2 flow of 25 mL min^{-1}. A reaction time of 30 min was used for Ag/SBA-15 NOMC, Ag/KIT-6 NOMC, and Ag/soft-NOMC.

To enhance the catalytic performance, we assessed the effect of changing the electrolyte from 0.5 M $KHCO_3$ to 0.5 M KOH using commercial Ag NPs, as it had been proven to provide two advantages. Firstly, the cell's ohmic resistance decreased, attributed to the more efficient dissociation of KOH into its constituent ions, K^+ and, OH^-. Additionally, the shift in pH from 8.6 for $KHCO_3$ to 14 for KOH had been demonstrated to be benefit the overpotential for the eCO_2RR.[50,51] When comparing both conditions for commercial Ag NPs with a loading of 0.2 mg cm^{-2}, the cell voltage dropped from -5.5 ± 0.2 V for 0.5 M $KHCO_3$ to -4.0 ± 0.1 V for 0.5 M KOH, resulting in improved energy efficiency while leaving the selectivity largely unaltered (*Fig.S19a-d, Supplementary information*). Subsequently, 0.5 M KOH was employed as the catholyte for the long-term evaluation of the optimized Ag/soft-NOMC samples (Ag/soft-NOMC/5 and Ag/soft-NOMC/10).

The optimized Ag/soft-NOMC catalysts were then compared to commercial Ag NPs (with a comparable Ag loading of 0.22 mg cm^{-2} determined by ICP-MS, as benchmark), a mixture of 5 wt% commercial Ag NPs and carbon black, a mixture of 5 wt% commercial Ag NPs and soft-NOMC (4.99 wt% determined by ICP-MS), synthesized Ag NPs deposited on a soft-NOMC structure in absence of thiourea (0.87 wt% determined by ICP-MS), and a blank soft-NOMC, shown in Figure 8a-b. The inclusion of carbon black with commercial Ag NPs highlighted the importance of an NOMC structure on the performance of the Ag NPs, as the presence of carbon black decreased the FE_{CO} by 51% while increasing the overpotential by 80 mV (*Fig S20, Supplementary information*). This decrease in CO selectivity was driven by the presence of carbon black in high amounts, which promoted the HER, resulting in a H_2 selectivity of 87 ± 4% at the end of the experiment. Subsequently, the mixture of commercial Ag NPs with a NOMC structure resulted in a 40% increase of the FE_{CO} compared to mixing with carbon black. This enhancement was mainly due to the nitrogen dopants in the carbon structure, improving CO selectivity in synergy with Ag NPs (see also Fig. 8), and reducing the overpotential by 130 mV, resulting in a comparable activity as commercial Ag NPs. The blank soft-NOMC, without the Ag NPs, already showed a selectivity of 19.0 ± 0.6% after 170 min, however the FE_{CO} took some time to reach this stable and higher value. This delay was likely due to the intricate pore network through which the CO_2 molecules had to diffuse, to reach and react on the N-doped active sites, as well as for the CO molecules to exit these pores. The incorporation of Ag NPs

to the soft-NOMC structure in absence of thiourea resulted in a considerable increase in FE_{CO} as compared to the bare NOMC but the FE's didn't reach the levels of those samples prepared with thiourea. Consequently, the soft-NOMC still showed high contribution in the observed FE since the hydrogen and formate trend were similar for both the blank soft-NOMC and the Ag/soft-NOMC/10NT.Moreover, the effects of degradation could not be observed due to the low loading of the sample (no clear Ag signal and particles were found with HAADF-STEM).

These results underscore the positive effect of mixing the Ag NPs with a nitrogen-doped carbon structure. Further improvements were achieved with the optimized Ag/soft-NOMC catalysts. The selectivity and the activity remained similar to the Com Ag/soft-NOMC/5 as a consequence of the comparable combination of NOMC structure, and Ag NPs (*Figure S21, Supporting information*). However, the stability of the catalyst emerged as a key parameter to comprehend the importance of an anchoring agent.

As shown in Figure 8c-d, the Ag/soft-NOMC catalysts maintained stability over the 6-hour experiment, while mixtures of commercial Ag NPs with the soft-NOMC structure started to exhibit a decrease in CO selectivity after 250 min. The decrease in FE_{CO} was related to the decrease in amount of Ag determined via ICP-MS, which indicated a loss of 19% Ag from 4.99 wt% to 4.0 wt% after eCO_2RR analysis. These commercial Ag NPs lacked the stability proved by anchoring agents, allowing for more rapid degradation processes (Fig. 9).

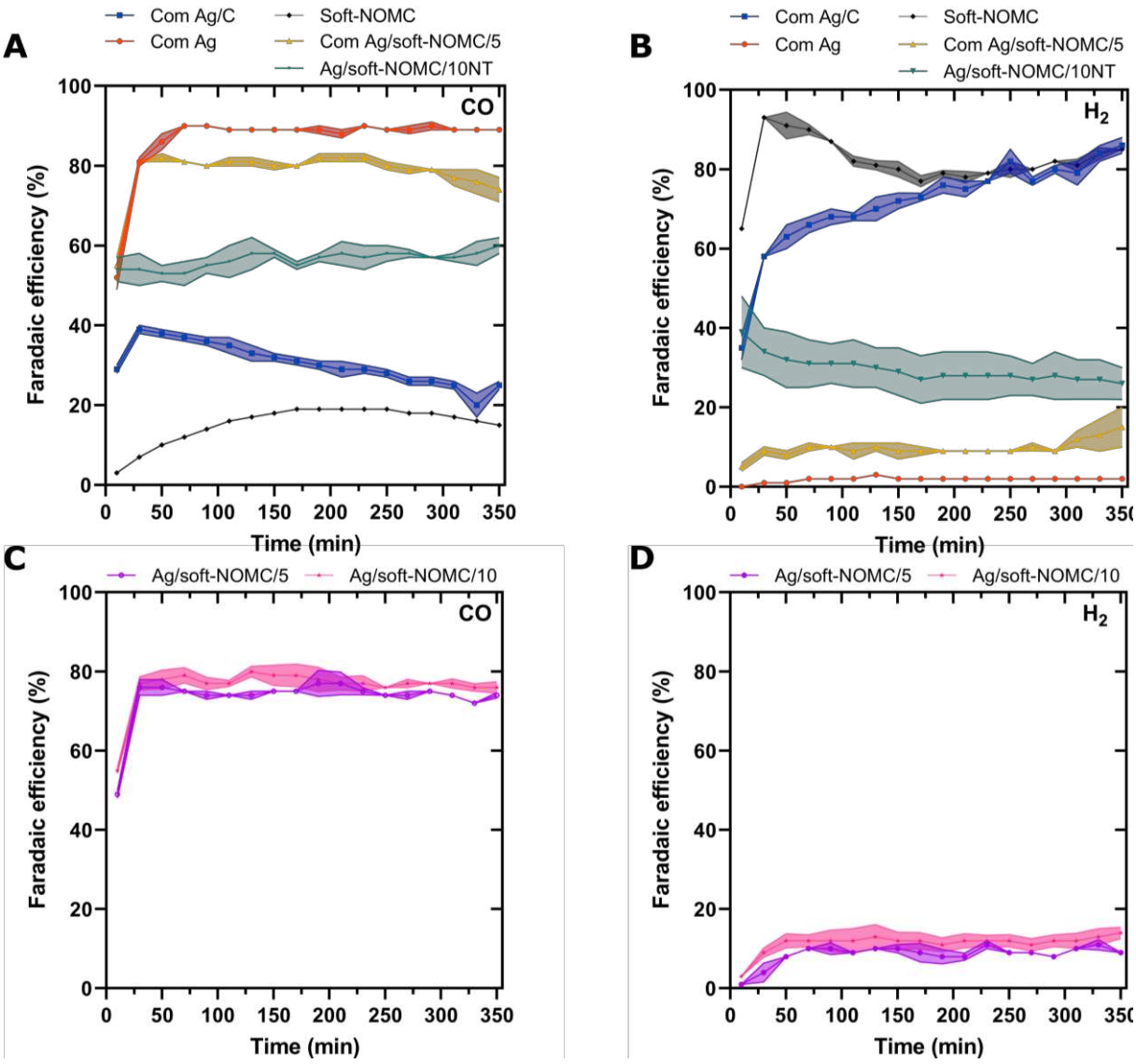

Figure 8: *(A) The average Faradaic efficiencies for CO and (B) H_2 for blank soft-NOMC (black), commercial Ag NPs (0.2 mg cm^{-2})(red), commercial Ag NPs mixed with carbon black (5 wt%) (blue), and commercial Ag NPs mixed with soft-NOMC (5 wt%) (yellow) and synthesized Ag NPs deposited onto the soft-NOMC structure without thiourea (Ag/soft-NOMC/10NT)(Teal). (C) The average Faradaic efficiencies for CO and (D) H_2 for Ag/soft-NOMC/5 (purple), and Ag/soft-NOMC/10 (pink) over 350 min in a small-scale flow-by electrolyzer at a current density of 100 mA cm^{-2} with 0.5 M KOH as catholyte, 2.0 M KOH as anolyte and a CO_2 flow of 25 mL min^{-1}. The remaining Faradaic efficiencies are assigned to formic acid resulting in a ~100% total Faradaic efficiency. The errors on the values are visualized by the band enclosing the data line. A reaction time of 5h was used for Ag/soft-NOMC/5, Ag/Soft-NOMC/10 and Ag/soft-NOMC/10NT.*

The main catalyst degradation processes influencing the selectivity are dissolution, Ostwald ripening, detachment, reshaping, fragmentation, and agglomeration. The addition of an

anchoring agent and their incorporation into the pores of the carbon support (nanoparticle confinement) limited the opportunity for the Ag NPs to undergo these degradation pathways.

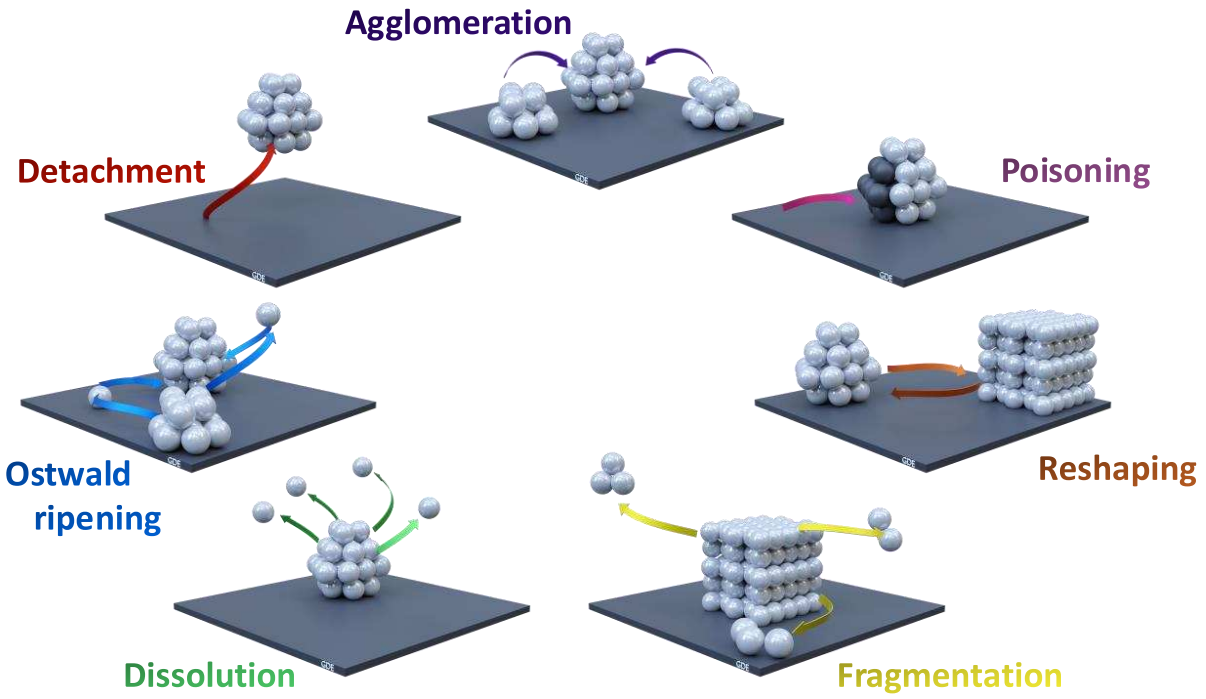

Figure 9: *Schematic overview of the various degradation pathways for an Ag catalyst.*

To prove this so-called nanoparticle confinement, the two optimized Ag/soft-NOMC catalysts were tested for 45 h and compared to the commercial Ag NPs (Fig 10a). The selectivity of the commercial Ag NPs initially remained around 90%, but it decreased noticeably during the experiment with an average rate of 0.022 % min^{-1} over 17.5 h. This trend remained until reaching a plateau at 15% after 55 h. The rapid decrease in FE_{CO} could be a combination of both reactor instability due to high probability of salt formation, electrowetting, and pressure change and catalysts degradation. Consequently, HAADF-STEM and ICP-MS was utilized to analyze the agglomeration and particle detachment, respectively. The ICP-MS data showed a lower Ag loading after, i.e. 155 µg cm^{-2} compared to 220 µg cm^{-2} before the long-term measurement of 72 h. Furthermore, HAADF-STEM and particle size distribution data clearly show a shift in average particle size from 29 ± 11 nm to 47 ± 16 nm. Additionally, after reaction a more pronounced presence of particles greater than 40 nm could be observed providing a decreased CO formation and increased HER *(Figure S22a-d, Supporting information)*.[40] Both observations clearly indicate the degradation of the commercial Ag NPs during reaction. The XRD pattern showed no alteration in the Ag crystallographic planes after the measurement with a consistent presence of (111) at 37.7°, (200) at 43.9°, (220) at 64.1° , and (311) at 77.0° *(Figure S23a-b, Supporting information)*. Nevertheless, the addition of peaks at 18.1°, 26.4°, and 54.5°

could be assigned to the crystallographic structure of $KHCO_3$ as a result of salt formation during the measurement. The effect of the salt formation in the GDE was further analyzed using CA measurements indicating a reduction in contact angle from 150° to 135° thus indicating a drop in hydrophobicity due to salt presence in the catalyst and MPL layer. Despite the presence of salts and the reduction in hydrophobicity, the contact angle remained above 90°, therefore, potential flooding will have probably been caused by electrowetting and change in pressure across the triple-phase boundary as observed in previous literature.[52] These reactor effects were also present during the analysis of the optimized Ag/soft-NOMC catalysts with identical effects visualized in the XRD patterns and the CA measurements*(Figure S23a-b, Figure S24a-f Supporting information)*. Despite this, the difference in catalyst stability was clear as a plateau was reached for the Ag/soft-NOMC catalysts. While they started at a lower selectivity of around 79% and 86% for the 5 wt % and 10 wt%, respectively, their decrease in performance was more gradually than for the commercial Ag NPs, which already indicates an improvement in stability as a result of the nanoparticle confinement strategy applied in this work. Moreover, the average rate of selectivity decrease was 0.008 % min^{-1} for Ag/soft-NOMC/5, almost a threefold improvement, while the Ag/soft-NOMC/10 showed more degradation effects with an average decrease of 0.016 % min^{-1} but still outperformed the commercial catalyst. The HAADF-STEM images, particle size distributions, and ICP-MS results support the higher stability of the synthesized Ag catalysts *(Figure S25a-d, Supporting information)*. Firstly, the particle size distribution of Ag/soft-NOMC/5 showed no significant shift in particle size, 12 ± 5 nm to 14 ± 5 nm, and the ICP-MS data showed only a reduction in Ag weight of 7.36 µg cm^{-2}. Furthermore, the Ag/soft-NOMC/10 with the presence of larger particles solely lost 29.83 µg cm^{-2}, while maintaining an average particle size of 17 ± 7 nm. Despite the fact that the Ag/soft-NOMC/5 and Ag/soft-NOMC/10 catalysts remained closer to their original structure, they still showed a decrease in selectivity towards CO, which is partially caused by the presence of some unanchored, and/or larger Ag NPs present at the external surface area being exposed to the degradation pathways mentioned previously. Despite the limited degradation, these results clearly show the benefits of anchoring as it has proven to be effective in reducing the detachment and agglomeration as such improving the overall durability of the system. Given the higher importance of stability from an economic point of view, we believe this strongly speaks in favor of using anchoring agents when using Ag to electrochemically reduce CO_2.

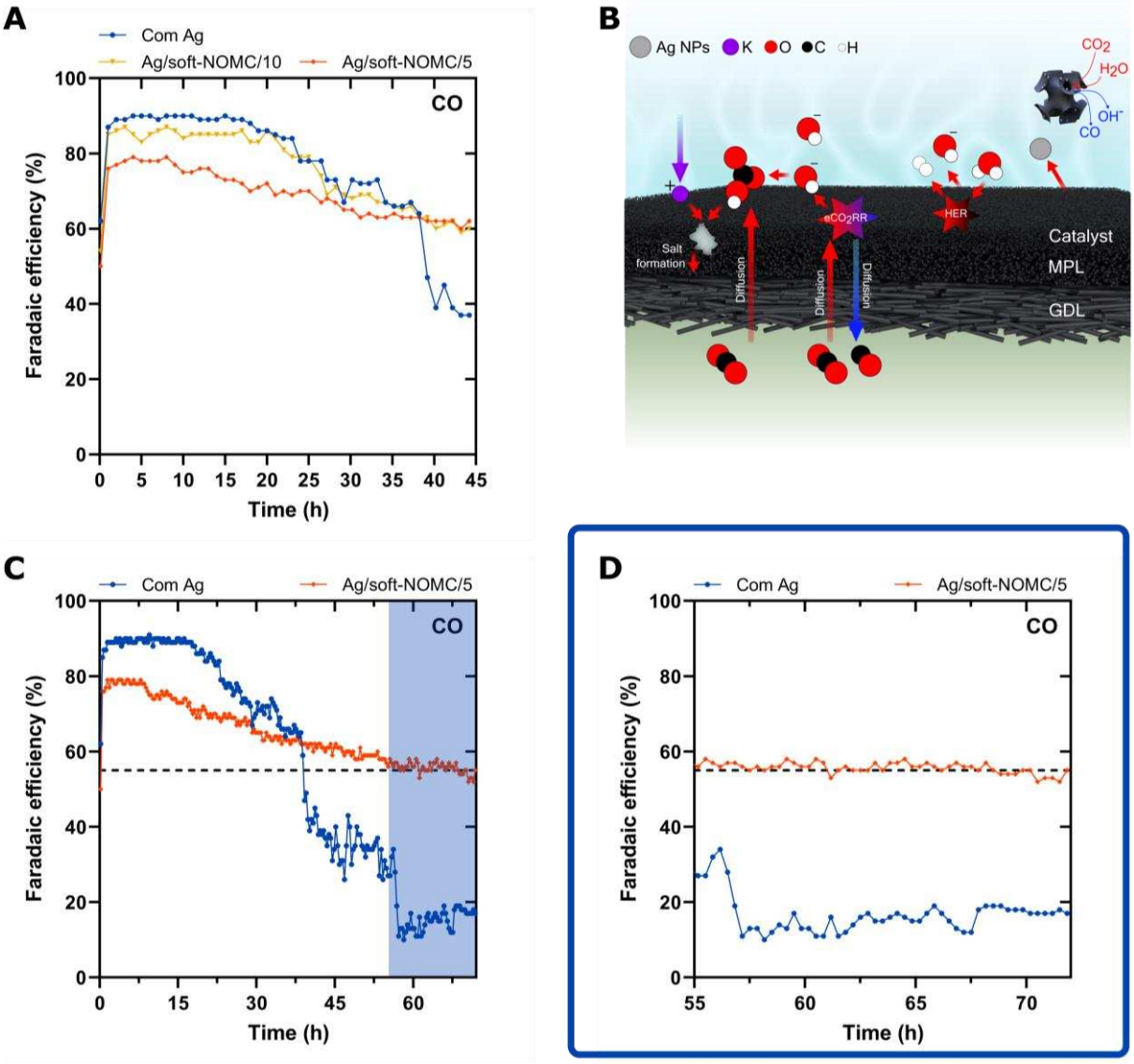

Figure 10: *(A) The Faradaic efficiencies for CO for commercial Ag NPs (0.2 mg cm^{-2})(blue), Ag/soft-NOMC/5 (red) and Ag/soft-NOMC/10 (yellow) over 45 hours.(B) Schematic overview of the eCO2RR in a flow-by electrolyzer with a GDE as substrate and Ag/soft-NOMC as catalyst. (C) the Faradaic efficiencies for CO for commercial Ag NPs (0.2 mg cm^{-2}) (blue), and Ag/soft-NOMC/5 (red) over 72 hours and (D) from 55 to 72 hours in a small-scale flow-by electrolyzer at a current density of 100 mA cm^{-2} with 0.5 M KOH as catholyte, 2.0 M KOH as anolyte and a CO_2 flow of 25 mL min^{-1}. The remaining Faradaic efficiencies are assigned to formic acid resulting in a ~100% total Faradaic efficiency. A reaction time of 5h was used for Ag/soft-NOMC/5, and Ag/soft-NOMC/10.*

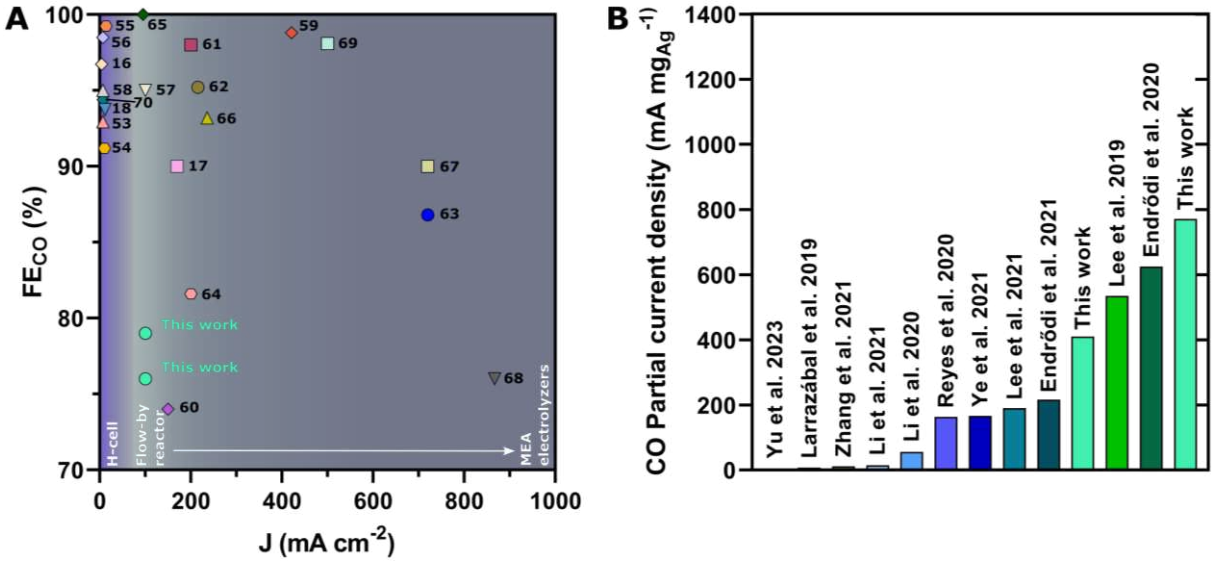

Figure 11: *(A) Literature overview of Ag-based catalysts for the eCO$_2$RR to CO in various electrochemical cells. (B) Comparison between various studies based on the amount of Ag employed, which is expressed as the CO partial current density (mA mg$_{Ag}^{-1}$).*[16–18,53–70]

The results were compared with recent studies on high-performance Ag-based catalysts for eCO$_2$RR to CO, as shown in Fig.11a. The synthesized Ag catalysts in this study have displayed a high FE towards CO, which are comparable to the high-performance Ag catalysts explored in literature. Nevertheless, the current density is still moderate in comparison to some of the more recent results. The utilization of a flow-by reactor allowed us to obtain improved current densities at similar overpotentials due to enhanced CO_2 mass-transfer compared to H-cells. Further increments in the current density were not explored since catalyst stability was the focus of this study. However, this catalyst has shown high promise compared to Ag-based catalysts used in literature due to the low amounts of Ag necessary to obtain high CO partial current densities (mA mg$_{Ag}^{-1}$) (Fig.11b). Consequently, these synthesized Ag-based catalysts could be of interest for membrane electrode assembly (MEA) systems where enhanced FE$_{CO}$ at higher current densities are obtained due to the absence of a catholyte which is known to contribute to the HER. Furthermore, additional improvements of these Ag/soft-NOMC catalysts such as large pores to increase the available surface area for deposition (larger chains of structure directing agents), higher weight percentage of pyridinic and pyrrolic nitrogen doping (fine-tuning the heat treatment step), and smaller particle size distribution, can still increase the activity, the selectivity, and the stability even further to also outperform the materials in literature in terms of initial activity and selectivity. Despite these proposed improvements, the concept of this study already showed the potential to deposit low amounts of nanoparticles on

a doped ordered mesoporous carbon for eCO_2RR and still be competitive with the other catalysts in the literature. Therefore, the findings obtained, showed the potential for large-scale synthesis of these catalysts while utilizing low amounts of metals, which remain confined within the supporting carbon framework throughout the measurement as such largely impeding the Ag NP degradation pathways.

4. CONCLUSION

The long-term stability and the loading of catalysts are major criteria to be considered for the industrial applicability of eCO_2RR catalysts, currently found in literature, remaining insufficient in either or one of both of these criteria. Therefore, this study proposed a new strategy to improve the stability of nanoparticles by anchoring them on- and into a doped OMC material, while minimizing the amount of catalyst required. By optimizing the Ag NPs size and interparticle distribution combined with a nitrogen-doped ordered mesoporous carbon support, a selectivity towards CO, ~80%, was achieved at industrially relevant current densities (100 mA cm^{-2}) using a loading of 10 wt% and less Ag. Furthermore, the anchoring of these Ag NPs provided an improved stability and increased the selectivity with 267% compared to commercial Ag NPs at the end of a long-term measurement of 72 h. This approach clearly shows the potential of incorporating active metal species into a doped ordered mesoporous carbon support for improving the durability. Further finetuning and optimizations are expected to continue to increase the overall durability. Additionally, this approach is not limited to Ag NPs but other metals can also be incorporated in the same manner, thereby expanding the product scope of this approach to other products including formate, ethylene, methane, etc. Even more so, this approach is not limited to the CO_2 reduction but could also be exploited in other electrochemical reactions where stability is an issue, e.g. water splitting, nitrogen/nitrate reduction, etc..

5. ASSOCIATED CONTENT

Supplementary information

Supplementary information is available in a separate file.

6. AUTHORS INFORMATION

Corresponding author

*Email: Tom.breugelmans@uantwerpen.be

Author contributions

The manuscript was written with contributions from all authors. All authors approved the final version of the manuscript.

7. ACKNOWLEDGEMENTS

The authors would like to acknowledge Catalisti VLAIO (Vlaanderen Agentschap Innoveren & Ondernemen) for their funding through the Moonshot SYN-CAT project (HBC.2020.2614). The funder played no role in the study design, data collection, analysis and interpretation of data, or the writing of this manuscript. Saskia Hoekx (ELCAT, UA, Belgium) acknowledges sponsoring from the research foundation of Flanders (FWO) in the frame of a doctoral grant (1S42623N). Sven Arnouts (ELCAT, UA, Belgium) acknowledges funding from the University of Antwerp Research fund (BOF). We thank Wouter Van Hoey, Karen Leyssens and Pegie Cool (LADCA, UA, Belgium) for helping with the XRD and N_2-physisorption measurements, Kitty Baert and Tom Hauffman (SURF, VUB, Belgium) for analyzing the samples with XPS and Raman, Hannelore Andries and Thomas Kenis for the ICP-MS measurements, and Barbara Bohlen (ELCAT, UA, Belgium) and Kavita Shivanagoud Patil (ELCAT, UA, Belgium) for the SEM and SEM-EDS measurements.

8. REFERENCES

(1) Kim, J.; Johnson, T. A.; Miller, J. E.; Stechel, E. B.; Maravelias, C. T. Fuel Production from CO2 Using Solar-Thermal Energy: System Level Analysis. *Energy Environ Sci* **2012**, *5* (9), 8417. https://doi.org/10.1039/c2ee21798h.

(2) Masson-Delmotte, V.; Zhai, P.; Pörtner, H.-O.; Roberts, D.; Skea, J.; Shukla, P. R.; Pirani, A.; Moufouma-Okia, W.; Péan, C.; Pidcock, R.; Connors, S.; Matthews, J. B. R.; Chen, Y.; Zhou, X.; Gomis, M. I.; Lonnoy, E.; Maycock, T.; Tignor, M.; Waterfield, T. *Global Warming of 1.5°C. An IPCC Special Report on the Impacts of Global Warming of 1.5°C above Pre-Industrial Levels and Related Global Greenhouse Gas Emission Pathways, in the Context of Strengthening the Global Response to the Threat of Climate Change, Sustainable Development, and Efforts to Eradicate Poverty*; 2018.

(3) Kätelhön, A.; Meys, R.; Deutz, S.; Suh, S.; Bardow, A. Climate Change Mitigation Potential of Carbon Capture and Utilization in the Chemical Industry. *Proc Natl Acad Sci U S A* **2019**, *166* (23), 11187–11194. https://doi.org/10.1073/pnas.1821029116.

(4) Wachsmuth, J.; Schaeffer, M.; Hare, B. The EU Long-Term Strategy to Reduce GHG Emissions in Light of the Paris Agreement and the IPCC Special Report on 1.5°C. *In Working Paper Sustainability and Innovation* **2018**, *S22*, 1–26.

(5) Kortlever, R.; Shen, J.; Schouten, K. J. P.; Calle-Vallejo, F.; Koper, M. T. M. Catalysts and Reaction Pathways for the Electrochemical Reduction of Carbon Dioxide. *Journal of Physical Chemistry Letters* **2015**, *6* (20), 4073–4082. https://doi.org/10.1021/acs.jpclett.5b01559.

(6) Vasileff, A.; Zheng, Y.; Qiao, S. Z. Carbon Solving Carbon's Problems: Recent Progress of Nanostructured Carbon-Based Catalysts for the Electrochemical Reduction of CO2. *Advanced Energy Materials*. Wiley-VCH Verlag November 8, 2017. https://doi.org/10.1002/aenm.201700759.

(7) Spurgeon, J. M.; Kumar, B. A Comparative Technoeconomic Analysis of Pathways for Commercial Electrochemical CO2 Reduction to Liquid Products. *Energy Environ Sci* **2018**, *11* (6), 1536–1551. https://doi.org/10.1039/c8ee00097b.

(8) Qi, J.; Finzel, J.; Robatjazi, H.; Xu, M.; Hoffman, A. S.; Bare, S. R.; Pan, X.; Christopher, P. Selective Methanol Carbonylation to Acetic Acid on Heterogeneous Atomically Dispersed ReO4/SiO2Catalysts. *J Am Chem Soc* **2020**, *142* (33), 14178–14189. https://doi.org/10.1021/jacs.0c05026.

(9) Maitlis, P. M.; Haynes, A.; Sunley, G. J.; Howard, M. J. Methanol Carbonylation Revisited: Thirty Years On. *Journal of the Chemical Society, Dalton Transactions* **1996**, No. 11, 2187. https://doi.org/10.1039/dt9960002187.

(10) Dyson, G. Malcolm. Phosgene. *Chem Rev* **1927**, *4* (1), 109–165. https://doi.org/10.1021/cr60013a003.

(11) Hietala, J.; Vuori, A.; Johnsson, P.; Pollari, I.; Reutemann, W.; Kieczka, H. *Ullmann's Encyclopedia of Industrial Chemistry*, 6th ed.; Wiley: Weinheim, 2003. https://doi.org/10.1002/14356007.

(12) Alipour, Z.; Babu Borugadda, V.; Wang, H.; Dalai, A. K. Syngas Production through Dry Reforming: A Review on Catalysts and Their Materials, Preparation Methods and Reactor Type. *Chemical Engineering Journal* **2023**, *452*, 139416. https://doi.org/10.1016/j.cej.2022.139416.

(13) Gotti, A.; Prins, R. Basic Metal Oxides as Cocatalysts for Cu/SiO2Catalysts in the Conversion of Synthesis Gas to Methanol. *J Catal* **1998**, *178* (2), 511–519. https://doi.org/10.1006/jcat.1998.2167.

(14) Hu, X.; Zhao, C.; Hu, X.; Guan, Q.; Wang, Y.; Li, W. Nitrogen-Doped Carbon Cages Encapsulating CuZn Alloy for Enhanced CO2 Reduction. *ACS Appl Mater Interfaces* **2019**, *11* (28), 25100–25107. https://doi.org/10.1021/acsami.9b03488.

(15) Li, X.; Bi, W.; Chen, M.; Sun, Y.; Ju, H.; Yan, W.; Zhu, J.; Wu, X.; Chu, W.; Wu, C.; Xie, Y. Exclusive Ni-N4 Sites Realize Near-Unity CO Selectivity for Electrochemical CO2 Reduction. *J Am Chem Soc* **2017**, *139* (42), 14889–14892. https://doi.org/10.1021/jacs.7b09074.

(16) Peng, X.; Karakalos, S. G.; Mustain, W. E. Preferentially Oriented Ag Nanocrystals with Extremely High Activity and Faradaic Efficiency for CO2 Electrochemical Reduction to CO. *ACS Appl Mater Interfaces* **2018**, *10* (2), 1734–1742. https://doi.org/10.1021/acsami.7b16164.

(17) Dinh, C. T.; García De Arquer, F. P.; Sinton, D.; Sargent, E. H. High Rate, Selective, and Stable Electroreduction of Co2 to Co in Basic and Neutral Media. *ACS Energy Lett* **2018**, *3* (11), 2835–2840. https://doi.org/10.1021/acsenergylett.8b01734.

(18) Li, Y.; Chen, C.; Cao, R.; Pan, Z.; He, H.; Zhou, K. Dual-Atom Ag2/Graphene Catalyst for Efficient Electroreduction of CO2 to CO. *Appl Catal B* **2020**, *268*. https://doi.org/10.1016/j.apcatb.2020.118747.

(19) He, Q.; Lee, J. H.; Liu, D.; Liu, Y.; Lin, Z.; Xie, Z.; Hwang, S.; Kattel, S.; Song, L.; Chen, J. G. Accelerating CO2 Electroreduction to CO Over Pd Single-Atom Catalyst. *Adv Funct Mater* **2020**, *30* (17). https://doi.org/10.1002/adfm.202000407.

(20) Zhu, W.; Kattel, S.; Jiao, F.; Chen, J. G. Shape-Controlled CO2 Electrochemical Reduction on Nanosized Pd Hydride Cubes and Octahedra. *Adv Energy Mater* **2019**, *9* (9). https://doi.org/10.1002/aenm.201802840.

(21) Chang, Q.; Kim, J.; Lee, J. H.; Kattel, S.; Chen, J. G.; Choi, S. il; Chen, Z. Boosting Activity and Selectivity of CO2 Electroreduction by Pre-Hydridizing Pd Nanocubes. *Small* **2020**, *16* (49). https://doi.org/10.1002/smll.202005305.

(22) Todoroki, N.; Tei, H.; Tsurumaki, H.; Miyakawa, T.; Inoue, T.; Wadayama, T. Surface Atomic Arrangement Dependence of Electrochemical CO2 Reduction on Gold: Online Electrochemical Mass Spectrometric Study on Low-Index Au(Hkl) Surfaces. *ACS Catal* **2019**, *9* (2), 1383–1388. https://doi.org/10.1021/acscatal.8b04852.

(23) Sun, K.; Shi, Y.; Li, H.; Shan, J.; Sun, C.; Wu, Z. yu; Ji, Y.; Wang, Z. Efficient CO2 Electroreduction via Au-Complex Derived Carbon Nanotube Supported Au Nanoclusters. *ChemSusChem* **2021**, *14* (22), 4929–4935. https://doi.org/10.1002/cssc.202101972.

(24) Yang, D. R.; Liu, L.; Zhang, Q.; Shi, Y.; Zhou, Y.; Liu, C.; Wang, F. bin; Xia, X. H. Importance of Au Nanostructures in CO2 Electrochemical Reduction Reaction. *Sci Bull (Beijing)* **2020**, *65* (10), 796–802. https://doi.org/10.1016/j.scib.2020.01.015.

(25) Luo, W.; Zhang, J.; Li, M.; Züttel, A. Boosting CO Production in Electrocatalytic CO2 Reduction on Highly Porous Zn Catalysts. *ACS Catal* **2019**, *9* (5), 3783–3791. https://doi.org/10.1021/acscatal.8b05109.

(26) Geng, Z.; Kong, X.; Chen, W.; Su, H.; Liu, Y.; Cai, F.; Wang, G.; Zeng, J. Oxygen Vacancies in ZnO Nanosheets Enhance CO2 Electrochemical Reduction to CO. *Angewandte Chemie - International Edition* **2018**, *57* (21), 6054–6059. https://doi.org/10.1002/anie.201711255.

(27) Xiao, J.; Gao, M. R.; Liu, S.; Luo, J. L. Hexagonal Zn Nanoplates Enclosed by Zn(100) and Zn(002) Facets for Highly Selective CO2 Electroreduction to CO. *ACS Appl Mater Interfaces* **2020**, *12* (28), 31431–31438. https://doi.org/10.1021/acsami.0c06891.

(28) Jiang, X.; Li, H.; Xiao, J.; Gao, D.; Si, R.; Yang, F.; Li, Y.; Wang, G.; Bao, X. Carbon Dioxide Electroreduction over Imidazolate Ligands Coordinated with Zn(II) Center in ZIFs. *Nano Energy* **2018**, *52*, 345–350. https://doi.org/10.1016/j.nanoen.2018.07.047.

(29) Xue, D.; Xia, H.; Yan, W.; Zhang, J.; Mu, S. Defect Engineering on Carbon-Based Catalysts for Electrocatalytic CO2 Reduction. *Nano-Micro Letters*. Springer Science and Business Media B.V. January 1, 2021. https://doi.org/10.1007/s40820-020-00538-7.

(30) Feaster, J. T.; Shi, C.; Cave, E. R.; Hatsukade, T.; Abram, D. N.; Kuhl, K. P.; Hahn, C.; Nørskov, J. K.; Jaramillo, T. F. Understanding Selectivity for the Electrochemical Reduction of Carbon Dioxide to Formic Acid and Carbon Monoxide on Metal Electrodes. *ACS Catal* **2017**, *7* (7), 4822–4827. https://doi.org/10.1021/acscatal.7b00687.

(31) Zeng, Q.; Yang, G.; Chen, J.; Zhang, Q.; Liu, Z.; Qin, B.; Peng, F. Effects of Nitrogen and Oxygen on Electrochemical Reduction of CO2 in Nitrogen-Doped Carbon Black. *Carbon N Y* **2023**, *202*, 1–11. https://doi.org/10.1016/j.carbon.2022.10.038.

(32) Daems, N.; de Mot, B.; Choukroun, D.; van Daele, K.; Li, C.; Hubin, A.; Bals, S.; Hereijgers, J.; Breugelmans, T. Nickel-Containing N-Doped Carbon as Effective Electrocatalysts for the Reduction of CO2 to CO in a Continuous-Flow Electrolyzer. *Sustain Energy Fuels* **2020**, *4* (3), 1296–1311. https://doi.org/10.1039/c9se00814d.

(33) Li, J.; Zitolo, A.; Garcés-Pineda, F. A.; Asset, T.; Kodali, M.; Tang, P.; Arbiol, J.; Galán-Mascarós, J. R.; Atanassov, P.; Zenyuk, I. V.; Sougrati, M. T.; Jaouen, F. Metal Oxide Clusters on Nitrogen-Doped Carbon Are Highly Selective for CO2 Electroreduction to CO. *ACS Catal* **2021**, *11* (15), 10028–10042. https://doi.org/10.1021/acscatal.1c01702.

(34) Van Daele, K.; De Mot, B.; Pupo, M.; Daems, N.; Pant, D.; Kortlever, R.; Breugelmans, T. Sn-Based Electrocatalyst Stability: A Crucial Piece to the Puzzle for the Electrochemical CO2 Reduction toward Formic Acid. *ACS Energy Lett* **2021**, *6* (12), 4317–4327. https://doi.org/10.1021/acsenergylett.1c02049.

(35) Wang, G.-H.; Cao, Z.; Gu, D.; Pfänder, N.; Swertz, A.-C.; Spliethoff, B.; Bongard, H.-J.; Weidenthaler, C.; Schmidt, W.; Rinaldi, R.; Schüth, F. Nitrogen-Doped Ordered Mesoporous Carbon Supported Bimetallic PtCo Nanoparticles for Upgrading of

Biophenolics. *Angewandte Chemie* **2016**, *128* (31), 8996–9001. https://doi.org/10.1002/ange.201511558.

(36) Sheng, X.; Daems, N.; Geboes, B.; Kurttepeli, M.; Bals, S.; Breugelmans, T.; Hubin, A.; Vankelecom, I. F. J.; Pescarmona, P. P. N-Doped Ordered Mesoporous Carbons Prepared by a Two-Step Nanocasting Strategy as Highly Active and Selective Electrocatalysts for the Reduction of O2 to H2O2. *Appl Catal B* **2015**, *176–177*, 212–224. https://doi.org/10.1016/j.apcatb.2015.03.049.

(37) Daems, N.; Risplendi, F.; Baert, K.; Hubin, A.; Vankelecom, I. F. J.; Cicero, G.; Pescarmona, P. P. Doped Ordered Mesoporous Carbons as Novel, Selective Electrocatalysts for the Reduction of Nitrobenzene to Aniline. *J Mater Chem A Mater* **2018**, *6* (27), 13397–13411. https://doi.org/10.1039/c8ta01609g.

(38) Kim, C.; Jeon, H. S.; Eom, T.; Jee, M. S.; Kim, H.; Friend, C. M.; Min, B. K.; Hwang, Y. J. Achieving Selective and Efficient Electrocatalytic Activity for CO2 Reduction Using Immobilized Silver Nanoparticles. *J Am Chem Soc* **2015**, *137* (43), 13844–13850. https://doi.org/10.1021/jacs.5b06568.

(39) Designed Research; S, S. P. P.; Performed Research; S, Y. S. P. Reversing the Size-Dependence of Surface Plasmon Resonances. **2010**, *107* (33), 14530–14534. https://doi.org/10.1073/pnas.1007524107/-/DCSupplemental.

(40) Salehi-Khojin, A.; Jhong, H. R. M.; Rosen, B. A.; Zhu, W.; Ma, S.; Kenis, P. J. A.; Masel, R. I. Nanoparticle Silver Catalysts That Show Enhanced Activity for Carbon Dioxide Electrolysis. *Journal of Physical Chemistry C* **2013**, *117* (4), 1627–1632. https://doi.org/10.1021/jp310509z.

(41) Deng, X.; Alfonso, D.; Nguyen-Phan, T.-D.; Kauffman, D. R. Resolving the Size-Dependent Transition between CO2 Reduction Reaction and H2 Evolution Reaction Selectivity in Sub-5 Nm Silver Nanoparticle Electrocatalysts. *ACS Catal* **2022**, *12* (10), 5921–5929. https://doi.org/10.1021/acscatal.2c00960.

(42) Ma, Q.; Fang, X.; Zhang, J.; Zhu, L.; Rao, X.; Lu, Q.; Sun, Z.; Yu, H.; Zhang, Q. Discrimination of Cysteamine from Mercapto Amino Acids through Isoelectric Point-Mediated Surface Ligand Exchange of β-Cyclodextrin-Modified Gold Nanoparticles. *J Mater Chem B* **2020**, *8* (18), 4039–4045. https://doi.org/10.1039/d0tb00462f.

(43) Noh, H. B.; Rahman, M. A.; Yang, J. E.; Shim, Y. B. Ag(I)-Cysteamine Complex Based Electrochemical Stripping Immunoassay: Ultrasensitive Human IgG Detection. *Biosens Bioelectron* **2011**, *26* (11), 4429–4435. https://doi.org/10.1016/j.bios.2011.04.058.

(44) Asadzadeh-Firouzabadi, A.; Zare, H. R. Application of Cysteamine-Capped Gold Nanoparticles for Early Detection of Lung Cancer-Specific MiRNA (MiR-25) in Human Blood Plasma. *Analytical Methods* **2017**, *9* (25), 3852–3861. https://doi.org/10.1039/c7ay01098b.

(45) Kuśmierek, K.; Borucka, M.; Świątkowski, A.; Dąbek, L. Evaluation of Different Carbon Materials in Adsorption and Solid-Phase Microextraction of 2,4,6-Trichlorophenol from Water. *Desalination Water Treat* **2019**, *157*, 129–137. https://doi.org/10.5004/dwt.2019.24124.

(46) Kou, W.; Zhang, Y.; Dong, J.; Mu, C.; Xu, L. Nickel-Nitrogen-Doped Three-Dimensional Ordered Macro-/Mesoporous Carbon as an Efficient Electrocatalyst for CO2 Reduction to CO. *ACS Appl Energy Mater* **2020**, *3* (2), 1875–1882. https://doi.org/10.1021/acsaem.9b02324.

(47) Wu, J.; Yadav, R. M.; Liu, M.; Sharma, P. P.; Tiwary, C. S.; Ma, L.; Zou, X.; Zhou, X. D.; Yakobson, B. I.; Lou, J.; Ajayan, P. M. Achieving Highly Efficient, Selective, and Stable CO2 Reduction on Nitrogen-Doped Carbon Nanotubes. *ACS Nano* **2015**, *9* (5), 5364–5371. https://doi.org/10.1021/acsnano.5b01079.

(48) Pacquets, L.; Van den Hoek, J.; Arenas-Esteban, D.; Ciocarlan, R.-G.; Cool, P.; Baert, K.; Hauffman, T.; Daems, N.; Bals, S.; Breugelmans, T. Use of Nanoscale Carbon Layers on Ag-Based Gas Diffusion Electrodes to Promote CO Production. *ACS Appl Nano Mater* **2022**, *5* (6), 7723–7732. https://doi.org/10.1021/acsanm.2c00473.

(49) Back, S.; Yeom, M. S.; Jung, Y. Active Sites of Au and Ag Nanoparticle Catalysts for CO2 Electroreduction to CO. *ACS Catal* **2015**, *5* (9), 5089–5096. https://doi.org/10.1021/acscatal.5b00462.

(50) Bhargava, S. S.; Proietto, F.; Azmoodeh, D.; Cofell, E. R.; Henckel, D. A.; Verma, S.; Brooks, C. J.; Gewirth, A. A.; Kenis, P. J. A. System Design Rules for Intensifying the Electrochemical Reduction of CO2 to CO on Ag Nanoparticles. *ChemElectroChem* **2020**, *7* (9), 2001–2011. https://doi.org/10.1002/celc.202000089.

(51) Kim, B.; Ma, S.; Molly Jhong, H. R.; Kenis, P. J. A. Influence of Dilute Feed and PH on Electrochemical Reduction of CO2 to CO on Ag in a Continuous Flow Electrolyzer. *Electrochim Acta* **2015**, *166*, 271–276. https://doi.org/10.1016/j.electacta.2015.03.064.

(52) Baumgartner, L. M.; Koopman, C. I.; Forner-Cuenca, A.; Vermaas, D. A. When Flooding Is Not Catastrophic–Woven Gas Diffusion Electrodes Enable Stable CO2Electrolysis. *ACS Appl Energy Mater* **2022**, *5* (12), 15125–15135. https://doi.org/10.1021/acsaem.2c02783.

(53) Fan, T.; Wu, Q.; Yang, Z.; Song, Y.; Zhang, J.; Huang, P.; Chen, Z.; Dong, Y.; Fang, W.; Yi, X. Electrochemically Driven Formation of Sponge-Like Porous Silver Nanocubes Toward Efficient CO2 Electroreduction to CO. *ChemSusChem* **2020**, *13* (10), 2677–2683. https://doi.org/10.1002/cssc.201903558.

(54) Zhang, W.; Zhu, N.; Ding, L.; Hu, Y.; Wu, Z. Efficacious CO2 Adsorption and Activation on Ag Nanoparticles/CuO Mesoporous Nanosheets Heterostructure for CO2 Electroreduction to CO. *Inorg Chem* **2021**, *60* (24), 19356–19364. https://doi.org/10.1021/acs.inorgchem.1c03183.

(55) Fu, H. Q.; Zhang, L.; Zheng, L. R.; Liu, P. F.; Zhao, H.; Yang, H. G. Enhanced CO2 Electroreduction Performance over Cl-Modified Metal Catalysts. *J Mater Chem A Mater* **2019**, *7* (20), 12420–12425. https://doi.org/10.1039/c9ta02223f.

(56) Park, J. Y.; Dong, W. J.; Lee, J. L. Monolithic Cl-Modified Nanoporous Ag Nanowires for Electrochemical CO2 Reduction to CO. *ACS Appl Energy Mater* **2022**, *5* (2), 1627–1634. https://doi.org/10.1021/acsaem.1c03043.

(57) Zhou, Y.; Ni, G.; Wu, K.; Chen, Q.; Wang, X.; Zhu, W.; He, Z.; Li, H.; Fu, J.; Liu, M. Porous Zn Conformal Coating on Dendritic-Like Ag with Enhanced Selectivity and Stability for CO2 Electroreduction to CO. *Adv Sustain Syst* **2023**, *7* (1). https://doi.org/10.1002/adsu.202200374.

(58) Yu, W.; Chen, S.; Zhu, J.; He, Z.; Song, S. A Highly Dispersed and Surface-Active Ag-BTC Catalyst with State-of-the-Art Selectivity in CO2 Electroreduction towards CO. *Journal of CO2 Utilization* **2023**, *70*. https://doi.org/10.1016/j.jcou.2023.102457.

(59) Ye, K.; Liu, T.; Song, Y.; Wang, Q.; Wang, G. Tailoring the Interactions of Heterogeneous Ag2S/Ag Interface for Efficient CO2 Electroreduction. *Appl Catal B* **2021**, *296*. https://doi.org/10.1016/j.apcatb.2021.120342.

(60) Haas, T.; Krause, R.; Weber, R.; Demler, M.; Schmid, G. Technical Photosynthesis Involving CO2 Electrolysis and Fermentation. *Nat Catal* **2018**, *1* (1), 32–39. https://doi.org/10.1038/s41929-017-0005-1.

(61) Larrazábal, G. O.; Strøm-Hansen, P.; Heli, J. P.; Zeiter, K.; Therkildsen, K. T.; Chorkendorff, I.; Seger, B. Analysis of Mass Flows and Membrane Cross-over in CO2 Reduction at High Current Densities in an MEA-Type Electrolyzer. *ACS Appl Mater Interfaces* **2019**, *11* (44), 41281–41288. https://doi.org/10.1021/acsami.9b13081.

(62) Lee, J.; Lim, J.; Roh, C. W.; Whang, H. S.; Lee, H. Electrochemical CO2 Reduction Using Alkaline Membrane Electrode Assembly on Various Metal Electrodes. *Journal of CO2 Utilization* **2019**, *31*, 244–250. https://doi.org/10.1016/j.jcou.2019.03.022.

(63) Endrődi, B.; Kecsenovity, E.; Samu, A.; Halmágyi, T.; Rojas-Carbonell, S.; Wang, L.; Yan, Y.; Janáky, C. High Carbonate Ion Conductance of a Robust PiperION Membrane Allows Industrial Current Density and Conversion in a Zero-Gap Carbon Dioxide Electrolyzer Cell. *Energy Environ Sci* **2020**, *13* (11), 4098–4105. https://doi.org/10.1039/d0ee02589e.

(64) Reyes, A.; Jansonius, R. P.; Mowbray, B. A. W.; Cao, Y.; Wheeler, D. G.; Chau, J.; Dvorak, D. J.; Berlinguette, C. P. Managing Hydration at the Cathode Enables Efficient CO2Electrolysis at Commercially Relevant Current Densities. *ACS Energy Lett* **2020**, *5* (5), 1612–1618. https://doi.org/10.1021/acsenergylett.0c00637.

(65) Lee, W. H.; Ko, Y. J.; Choi, Y.; Lee, S. Y.; Choi, C. H.; Hwang, Y. J.; Min, B. K.; Strasser, P.; Oh, H. S. Highly Selective and Scalable CO2 to CO - Electrolysis Using Coral-Nanostructured Ag Catalysts in Zero-Gap Configuration. *Nano Energy* **2020**, *76*. https://doi.org/10.1016/j.nanoen.2020.105030.

(66) Xu, Y.; Edwards, J. P.; Liu, S.; Miao, R. K.; Huang, J. E.; Gabardo, C. M.; O'Brien, C. P.; Li, J.; Sargent, E. H.; Sinton, D. Self-Cleaning CO2Reduction Systems: Unsteady Electrochemical Forcing Enables Stability. *ACS Energy Lett* **2021**, *6* (2), 809–815. https://doi.org/10.1021/acsenergylett.0c02401.

(67) Endrődi, B.; Samu, A.; Kecsenovity, E.; Halmágyi, T.; Sebők, D.; Janáky, C. Operando Cathode Activation with Alkali Metal Cations for High Current Density Operation of Water-Fed Zero-Gap Carbon Dioxide Electrolysers. *Nat Energy* **2021**, *6* (4), 439–448. https://doi.org/10.1038/s41560-021-00813-w.

(68) Ye, K.; Zhang, G.; Ma, X.-Y.; Deng, C.; Huang, X.; Yuan, C.; Meng, G.; Cai, W.-B.; Jiang, K. Resolving Local Reaction Environment toward an Optimized CO 2-to-CO Conversion Performance. *Energy Environ Sci* **2022**, *15* (2), 749–759. https://doi.org/10.1039/D1EE02966E.

(69) Li, S.; Dong, X.; Zhao, Y.; Mao, J.; Chen, W.; Chen, A.; Song, Y.; Li, G.; Jiang, Z.; Wei, W.; Sun, Y. Chloride Ion Adsorption Enables Ampere-Level CO2 Electroreduction over Silver Hollow Fiber. *Angewandte Chemie - International Edition* **2022**, *61* (42). https://doi.org/10.1002/anie.202210432.

(70) Li, C.; Xiong, H.; He, M.; Xu, B.; Lu, Q. Oxyhydroxide Species Enhances CO2Electroreduction to CO on Ag via Coelectrolysis with O2. *ACS Catal* **2021**, *11* (19), 12029–12037. https://doi.org/10.1021/acscatal.1c02852.